ARTICLES
https://doi.org/10.1038/s41556-020-0532-x

nature cell biology

Check for updates

Dissecting intratumour heterogeneity of nodal B-cell lymphomas at the transcriptional, genetic and drug-response levels

Tobias Roider[1,2,3], Julian Seufert[4,5], Alexey Uvarovskii[6], Felix Frauhammer[6], Marie Bordas[4,7], Nima Abedpour[8], Marta Stolarczyk[1], Jan-Philipp Mallm[9], Sophie A. Herbst[1,2,3,5,10], Peter-Martin Bruch[1,2,3], Hyatt Balke-Want[8], Michael Hundemer[1], Karsten Rippe[9], Benjamin Goeppert[11], Martina Seiffert[7], Benedikt Brors[12], Gunhild Mechtersheimer[11], Thorsten Zenz[13], Martin Peifer[8], Björn Chapuy[14], Matthias Schlesner[4], Carsten Müller-Tidow[1,2,3], Stefan Fröhling[10,15], Wolfgang Huber[2,3], Simon Anders[6,16] and Sascha Dietrich[1,2,3,10,16] ✉

Tumour heterogeneity encompasses both the malignant cells and their microenvironment. While heterogeneity between individual patients is known to affect the efficacy of cancer therapy, most personalized treatment approaches do not account for intratumour heterogeneity. We addressed this issue by studying the heterogeneity of nodal B-cell lymphomas by single-cell RNA-sequencing and transcriptome-informed flow cytometry. We identified transcriptionally distinct malignant subpopulations and compared their drug-response and genomic profiles. Malignant subpopulations from the same patient responded strikingly differently to anti-cancer drugs ex vivo, which recapitulated subpopulation-specific drug sensitivity during in vivo treatment. Infiltrating T cells represented the majority of non-malignant cells, whose gene-expression signatures were similar across all donors, whereas the frequencies of T-cell subsets varied significantly between the donors. Our data provide insights into the heterogeneity of nodal B-cell lymphomas and highlight the relevance of intratumour heterogeneity for personalized cancer therapy.

The genomic and transcriptional landscape of many cancer entities has been catalogued over recent years, documenting the range of tumour heterogeneity between individual patients[1,2]. In addition, it has long been appreciated that the tumours in a patient consist of diverse but phylogenetically related subclones[3]. Bulk-sequencing studies have been conducted to infer the genetic spectrum of intratumour heterogeneity from the variant-allele frequencies of somatic mutations[4]. Non-malignant bystander cells represent another layer of heterogeneity, which support tumour growth[5] and affect the prognosis and response to treatment[6].

While bulk genomic tissue profiling has only a limited ability to reconstruct the complex cellular composition of tumours, single-cell DNA-[7,8] and RNA-sequencing (scRNA-seq)[9–13] have emerged as powerful tools to study intratumour heterogeneity and reconstruct the full picture of malignant and non-malignant cells. These technologies further enable researchers to identify rare cell types, such as cancer stem cells[14] and circulating tumour cells[15,16], or follow clonal dynamics during cancer treatment[17]. Most of these studies describe cell subpopulations on the transcriptional level but their functional properties, such as their drug-response profiles, remain largely unexplored.

To address this, we used B-cell non-Hodgkin lymphoma (B-NHL) as a model disease entity to dissect intratumour heterogeneity at the transcriptional, genetic and drug-response levels. The majority of B-NHLs grow in the lymph node compartment and almost half of them are classified as diffuse large B-cell lymphomas (DLBCLs), follicular lymphomas (FL) or transformed FLs[18,19]. Despite effective immunochemotherapy treatment options, relapses occur frequently[20,21] and the response to single-agent targeted therapy of these patients is surprisingly low[22,23]. Intratumour heterogeneity might be a key factor contributing to the therapeutic failure and low success rate of single-agent targeted therapies[4]. Understanding the subclonal drug-response patterns would therefore be an important asset for the design of more effective personalized lymphoma therapies.

[1]Department of Medicine V, Hematology, Oncology and Rheumatology, University of Heidelberg, Heidelberg, Germany. [2]Molecular Medicine Partnership Unit (MMPU), Heidelberg, Germany. [3]European Molecular Biology Laboratory (EMBL), Heidelberg, Germany. [4]Bioinformatics and Omics Data Analytics, German Cancer Research Center (DKFZ), Heidelberg, Germany. [5]Faculty of Biosciences, University of Heidelberg, Heidelberg, Germany. [6]Center for Molecular Biology of the University of Heidelberg (ZMBH), Heidelberg, Germany. [7]Division of Molecular Genetics, German Cancer Research Center (DKFZ), Heidelberg, Germany. [8]Department for Translational Genomics, University of Cologne, Cologne, Germany. [9]Division of Chromatin Networks, German Cancer Research Center (DKFZ) and Bioquant, Heidelberg, Germany. [10]Department of Translational Medical Oncology, National Center for Tumor Diseases (NCT) Heidelberg and German Cancer Research Center (DKFZ), Heidelberg, Germany. [11]Institute of Pathology, University of Heidelberg, Heidelberg, Germany. [12]Division of Applied Bioinformatics, German Cancer Research Center (DKFZ), Heidelberg, Germany. [13]Department of Medical Oncology and Hematology, University of Zürich, Zürich, Switzerland. [14]Clinic for Hematology and Medical Oncology, University Medicine Göttingen, Göttingen, Germany. [15]German Cancer Consortium (DKTK), Heidelberg, Germany. [16]These authors contributed equally: Simon Anders, Sascha Dietrich. ✉e-mail: sascha.dietrich@embl.de

To dissect the cellular composition of malignant lymph nodes, we profiled single-cell transcriptomes from 12 different reactive or B-NHL lymph-node biopsies and confirmed our findings by flow cytometry in a larger cohort of 41 patients. Among the malignant cells, we identified transcriptionally distinct malignant subpopulations and further characterized them by ex vivo drug perturbation and genome sequencing. This revealed insights into the intratumour heterogeneity of B-NHLs and demonstrated substantially different drug responses between malignant subpopulations in the same patient.

Results

Study outline. We designed an experimental pipeline to dissect the heterogeneity of non-malignant and malignant lymph node-derived lymphocytes (Fig. 1a). The subpopulations identified by scRNA-seq were validated by flow cytometry using distinguishing markers, and the subpopulations were finally functionally interrogated in drug perturbation assays and further characterized by whole-genome and/or -exome sequencing (WGS and WES, respectively).

Dissecting the cellular composition of nodal B-cell lymphomas. We assayed single-cell suspensions of 12 lymph node samples by flow cytometry and scRNA-seq (Supplementary Table 1): four germinal centre-derived DLBCLs, of which two were transformed from FLs (DLBCL1, DLBCL2, tFL1 and tFL2), one non-germinal centre-derived DLBCL (DLBCL3), four FL (FL1, FL2, FL3 and FL4) and three reactive non-malignant lymph node (rLN) samples (rLN1, rLN2 and rLN3).

We first verified that the lymph node-derived single-cell suspensions were representative of the cellular composition (B and T cells) of the lymphoma and its microenvironment. We used immunohistochemistry (IHC) to quantify the B- and T-cell frequencies in sections of paraffin-embedded and formalin-fixed lymph nodes (Extended Data Fig. 1a). In parallel, we determined the B- and T-cell frequencies using flow cytometry and scRNA-seq (Extended Data Fig. 1a,b). The frequencies of the B and T cells calculated using scRNA-seq correlated perfectly with the frequencies determined using flow cytometry (Pearson's correlation coefficient (r) = 0.97, n = 12; Fig. 1b) and IHC (r = 0.92, n = 7; Fig. 1c).

To further distinguish malignant from non-malignant B cells, we leveraged the fact that malignant B-cell populations express only one type of immunoglobulin light chain—that is, either a κ or λ light chain[24]. We calculated the light chain ratio (κ/λ) for each B cell based on the scRNA expression of the genes *IGKC* (coding for the constant part of the κ light chain) and *IGLC2* (λ light chain) and colour-coded this ratio in a *t*-distributed stochastic neighbour-embedding (t-SNE) plot (Fig. 1d,e). In the malignant lymph nodes, we could identify either non-malignant and malignant or only malignant B-cell clusters (Extended Data Figs. 2 and 3a). In contrast, reactive lymph node samples contained only non-malignant B-cell clusters (see the Methods section for details).

We further evaluated the frequencies of these B-cell subsets in a larger cohort of 41 lymph node samples (Supplementary Table 1) by flow cytometry, including the samples used for scRNA-seq. Both approaches showed very similar frequencies of these cell subsets (r = 0.97, n = 12; Extended Data Fig. 3a,b). The proportion of malignant cells was highly variable across all of the studied disease entities (chronic lymphocytic leukaemia (CLL), mantle cell lymphoma (MCL), DLBCL and FL), ranging from 14.6 to 97.2% with a median of 76.8% (Extended Data Fig. 3c). This substantial cellular heterogeneity complicates bulk-sequencing approaches of unsorted lymph node samples and highlights the value of single-cell sequencing to simultaneously study the full spectrum of malignant and non-malignant lymph node cells.

Characterization of lymph node-derived T-cell populations. B-cell non-Hodgkin lymphomas exhibit genetic immune escape strategies that can be targeted using current therapeutic strategies[25,26], including checkpoint inhibitors[27] and bispecific antibodies[28]. Notably, lymphoma cells can also orchestrate their tumour microenvironment so that certain T-cell subsets support the tumour cells[29]. Although these subsets have been extensively studied by immunophenotyping, their transcriptional heterogeneity in B-NHL lymph nodes, in particular at the single-cell level, still needs to be elucidated.

We combined the single-cell transcriptomes of T cells from all 12 donors and jointly visualized them using Uniform Manifold Approximation and Projection (UMAP)[30]. Many of the well-established surface markers that are used to distinguish T-cell subsets by flow cytometry are insufficiently expressed on the scRNA level. We therefore chose unsupervised clustering to partition T cells into transcriptionally distinct subsets, which were then annotated by differentially expressed marker genes. All T cells from either reactive or malignant lymph nodes distributed to only four major T-cell subpopulations (Fig. 2a,b). Note that the clusters were not driven by the patients or disease entity, which suggests that there was only limited transcriptional heterogeneity across all donors. Apart from conventional T helper cells (T_H; *CD4*, *IL7R*, *PLAC8* and *KLF2*) and regulatory T cells (T_{REG}; *CD4*, *IL2RA*, *FOXP3* and *ICOS*), we identified a third T_H cell population characterized by overexpression of *PDCD1* (PD1), *ICOS*, *CXCR5*, *TOX*, *TOX2* and *CD200* (Fig. 2c and Supplementary Table 2), suggesting a T-follicular-helper-cell (T_{FH}) phenotype[31–35]. In contrast to the diversity of T_H cells, we observed only one cluster of cytotoxic T cells (T_{TOX}; *GZMK*, *CCL4/5*, *GZMA*, *NKG7* and *CD8A*).

To study the variable frequency of these four T-cell subsets (Fig. 2d) in a larger cohort, we analysed 40 lymph node samples of DLBCLs, FLs, MCLs and CLLs by flow cytometry using the most distinctive markers (CD3, CD4, CD8, CD25, FoxP3, ICOS and PD1; Fig. 2c). The frequencies of all T-cell subsets derived from the scRNA-seq correlated well with the frequencies determined using flow cytometry (r = 0.69, n = 10; Fig. 2e). We found that T_{FH} cells were significantly increased in FLs (two-sided Wilcoxon test, P = 0.006; Fig. 2f), which is in line with previous flow cytometry-based studies[35,36]. In addition, we found that the frequencies of T_{REG} cells were significantly increased in malignant lymph nodes compared with the reactive ones (two-sided Wilcoxon test, P values as indicated in Fig. 2f).

Together, our findings indicate that B-NHLs shape their microenvironment by influencing the recruitment of certain T-cell subpopulations but have less effect on their transcriptional programs.

Identification of gene-expression signatures driving B-cell heterogeneity by scRNA-seq. Next, we combined the single-cell transcriptomes of B cells from all 12 donors and jointly visualized them using UMAP (Fig. 3a,b). Clustering partitioned the non-malignant B cells into two distinct subpopulations (C0 and C1; Fig. 3a). Among the multiple genes that were differentially expressed between these two subsets (Supplementary Table 3), we found *IGHM* and *CD72* to be overexpressed in cluster C0, which characterizes naive B cells[37], and *CD27* and *IGHG1* to be overexpressed in cluster C1, which characterizes memory B cells[38].

Of the eight transcriptionally distinct clusters formed by the malignant B cells (C2–C9; Fig. 3a), six exclusively contained cells from only one donor (Fig. 3a,b), suggesting a higher degree of inter-patient heterogeneity of malignant compared with non-malignant B cells. A gene set enrichment analysis (GSEA) revealed multiple cluster-specific gene sets (Fig. 3c,d), such as germinal centre B cell-associated signatures, which were significantly enriched in all clusters except cluster 6, which exclusively contained malignant B cells from DLBCL3. This finding

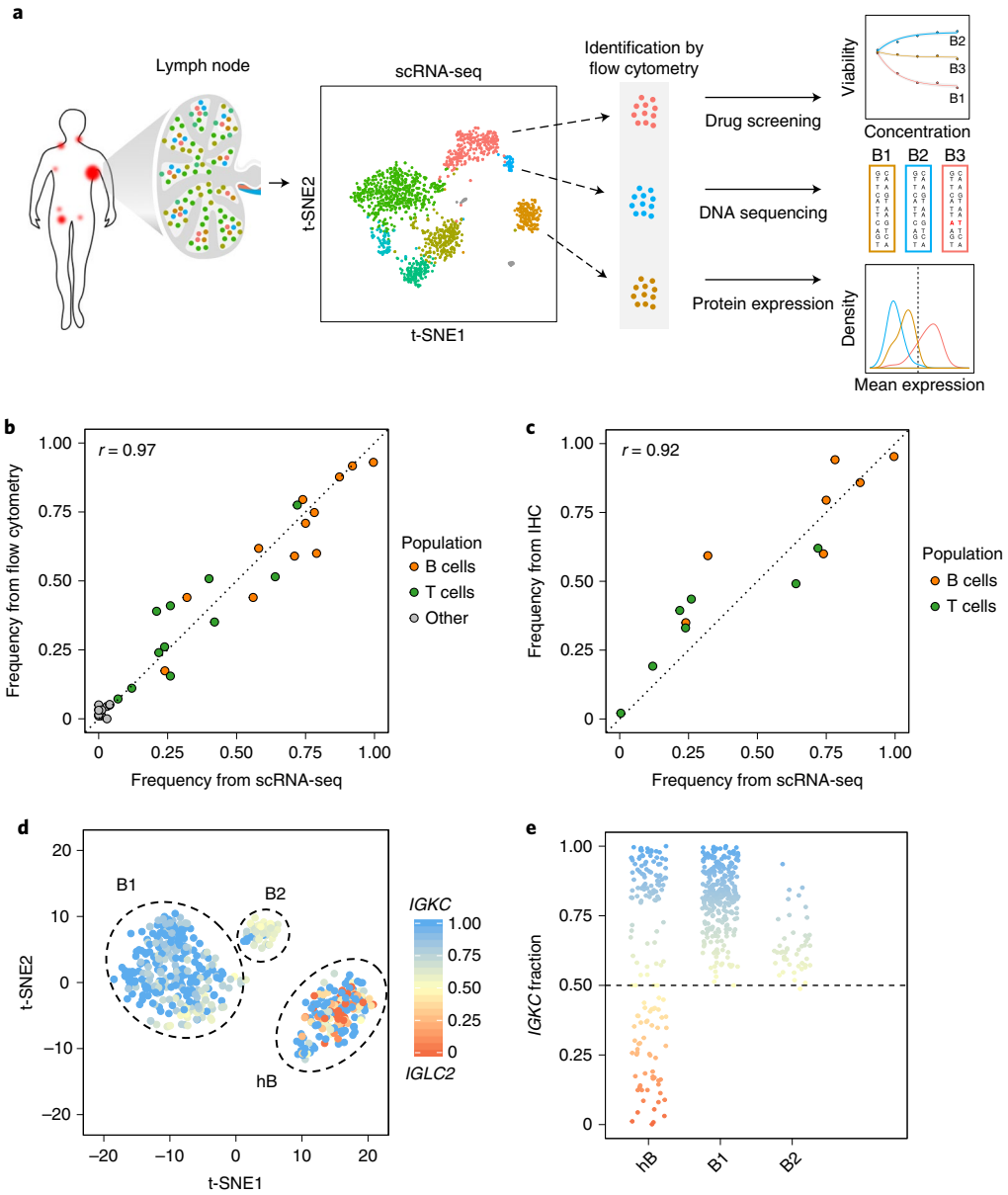

Fig. 1 | Identification of cell types using scRNA-seq. a, Schematic overview of the study design. **b**,**c**, Lymph node-derived B and T cells were quantified by scRNA-seq, flow cytometry and IHC of paraffin-embedded tissue sections (see Extended Data Fig. 1a). The frequencies of the B and T cells correlated between scRNA-seq and flow cytometry (**b**), and scRNA-seq and IHC (**c**). The Pearson's correlation coefficients are given for $n=12$ (**b**) and 7 (**c**) biologically independent samples. **d**,**e**, Illustration of the strategy used to identify malignant B cells by reference to a representative sample (tFL1, 492 cells) of a total of $n=12$ biologically independent samples. The legend applies to both panels. **d**, The scRNA expression profiles of the B cells were visualized by t-SNE. The different B-cell clusters are circled and labelled. **e**, The *IGKC* fraction, *IGKC* ÷ (*IGKC* + *IGLC2*), was calculated for each B cell. If the *IGKC* fraction was >0.5, we classified a B cell as κ^+, and if this ratio was below 0.5, we classified the B cell as λ^+. The percentage of B cells expressing either κ or λ was calculated per transcriptionally distinct B-cell cluster. The non-malignant healthy B-cell cluster contained approximately 50% κ- and 50% λ-expressing B cells, whereas the tow malignant clusters (B1 and B2) contained B cells homogeneously expressing the κ light chain. B1, B-cell cluster 1; B2, B-cell cluster 2; and hB, healthy B cells. The statistical source data are provided.

supports the IHC-based classification of DLBCL3 as a non-germinal centre B-cell lymphoma subtype[39] (Supplementary Table 1). Individual clusters were characterized by oncogenic transcriptional programs, which indicated activation of oncogenic MYC and STK33 signalling (Fig. 3d).

Inter-patient heterogeneity of B-cell lymphomas also comprises their proliferative capacity, which can vary from very low in FLs to very high in DLBCLs. The proportion of B cells in the S, G_2 and M phases based on their scRNA profile (Extended Data Fig. 4a) correlated very well with the flow cytometry- and IHC-based staining of Ki67 (scRNA-seq to flow cytometry, $r=0.83$; and scRNA-seq to IHC, $r=0.92$; Extended Data Fig. 4b).

These results indicate that inter-patient heterogeneity of malignant B cells, including their diverse proliferative activity, can be captured by scRNA-seq and can be linked to lymphoma-specific transcription signatures. However, non-malignant B cells had similar transcriptional profiles across different donors.

Decoding the crosstalk between T cells and malignant B cells within the lymph node microenvironment. From the results

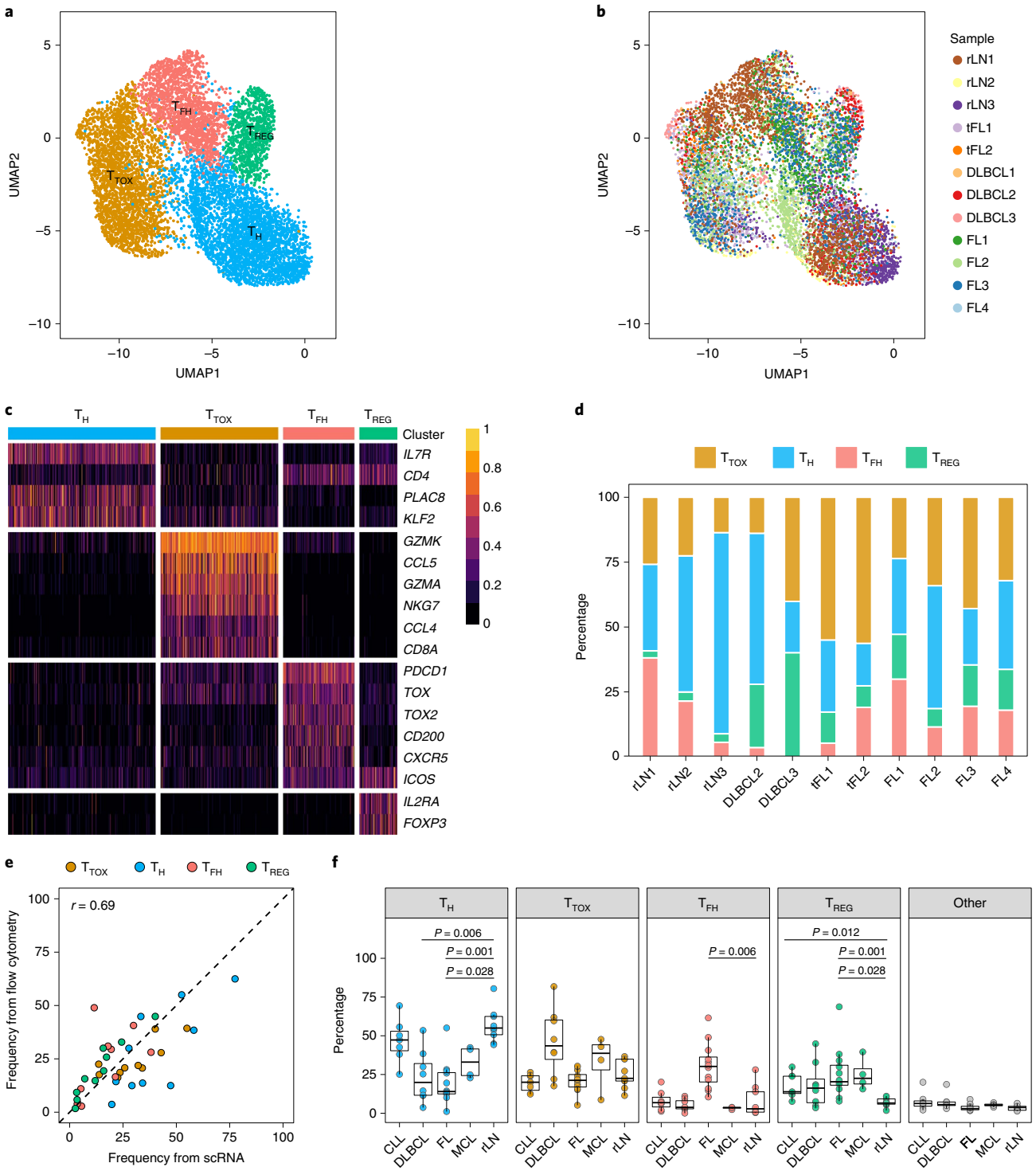

Fig. 2 | Transcriptional heterogeneity of lymph node-derived T cells. a,**b**, T cells from $n=12$ biologically independent samples were combined and jointly visualized using UMAP. The cells were coloured with respect to their cluster (**a**) or sample origin (**b**). **c**, Differentially expressed genes used to identify the T-cell subsets: T_{TOX}, conventional T_H, T_{FH} and T_{REG} cells. The gene-expression values were scaled to the maximum of each row. **d**, Proportion of T-cell subpopulations identified in each sample based on scRNA-seq. Note that the DLBCL1 sample is not shown here as only five T cells were identified in this sample. **e**,**f**, Lymph node cells derived from 40 different patients, including those passed to scRNA-seq, were characterized by flow cytometry. The four different T-cell populations identified by scRNA-seq were distinguished as follows: T_H, $CD3^+CD4^+$ cells lacking the T_{FH} and T_{REG} phenotype; T_{TOX}, $CD3^+CD8^+$ cells; T_{FH}, $CD3^+CD4^+ICOS^{High}PD1^{High}$ cells; and T_{REG}, $CD3^+CD4^+FoxP3^+$ cells. **e**, Correlation of the frequencies calculated using flow cytometry with those calculated using scRNA-seq. $n=10$ biologically independent samples. **f**, Frequencies of each subpopulation with regard to the sum of all T cells for $n=7$ (CLL), 8 (DLBCL), 12 (FL), 4 (MCL) and 9 (rLN) biologically independent samples. The P values were calculated using a two-sided Wilcoxon's test and corrected using Bonferroni's method. P values are only shown where $P \leq 0.05$ relative to the rLN group. The box plots show the minimum, first quartile, median, second quartile and maximum. Outliers defined as values higher or lower than 1.5× the interquartile ranges from the median are shown as individual dots. The statistical source data are provided.

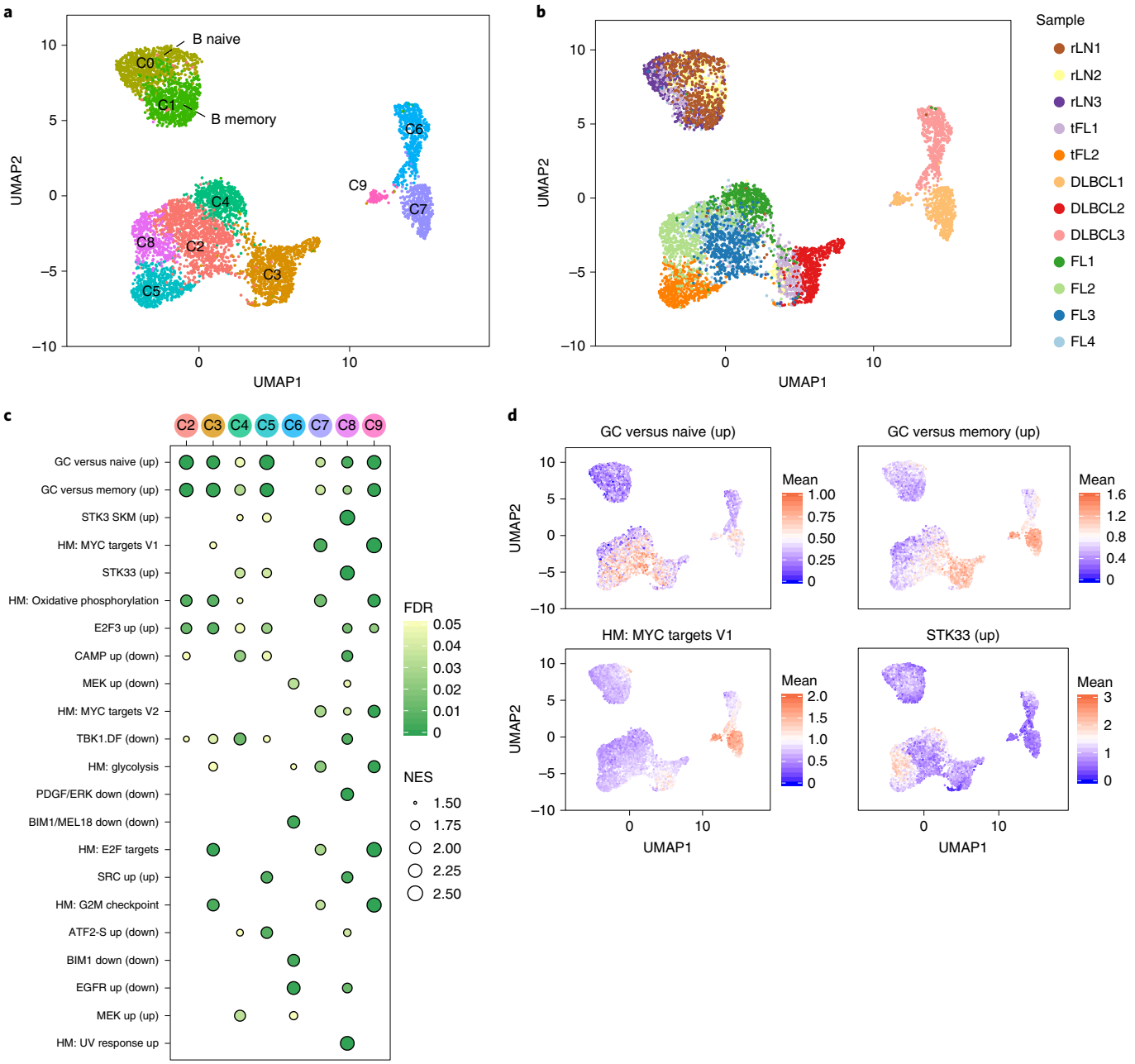

Fig. 3 | Gene-expression signatures driving B-cell heterogeneity. a–**d**, B cells from $n=12$ biologically independent samples were combined and jointly analysed. **a**,**b**, Cells were visualized using UMAP and coloured by shared nearest neighbour (SNN)-based clusters (**a**) or sample (**b**). **c**, A GSEA was performed separately for each malignant cluster (C3–C9) versus all healthy B cells (C0 and C1). The four most-enriched gene sets per sample are shown. The columns refer to the cluster annotation from **a**. The circles are coded by colour (nominal false-positive detection rate, FDR) and size (normalized enrichment score, NES). Only gene sets with NES > 1.5 are shown. The FDR and NES were calculated using the GSEA desktop application (see the Methods section for details). **d**, Cells in the UMAP plot (see **a**,**b**) were coloured by the mean expression of enriched genes for four representative gene-expression signatures. GC, germinal centre B cell. HM, hallmark. The statistical source data are provided.

mentioned earlier, we concluded that B-cell lymphomas shape their microenvironment by modulating the frequency of different subsets of lymphoma-infiltrating T cells. We next aimed to understand through which potential ligand–receptor interactions malignant B cells could benefit from their microenvironment. For this purpose, we adopted the computational approach described by Vento-Tormo et al.[40] to identify the most significant interactions between malignant B cells and lymphoma-infiltrating T cells (Fig. 4).

This analysis suggested that malignant B cells could receive costimulatory and coinhibitory signals from all four major T-cell subsets via CD80/CD86–CD28 and CD80/CD86–CTLA, whereas interactions via BCMA–BAFF, BAFF-R–BAFF and CD40–CD40LG could predominantly be mediated by T_H and T_{REG} cells. Significant interaction scores for the IL4–IL4R and IL4–IL13RA1 interactions were exclusively observed between T_{FH} and malignant B cells, providing further evidence that T_{FH} cells represent the most important source of IL4 in B-NHL[41]. This observation might be of clinical relevance because the IL4–IL4R interaction is discussed as a potential resistance mechanism against Bruton's tyrosine kinase (BTK) inhibitors[42,43]. In agreement with what is known at present[44–46],

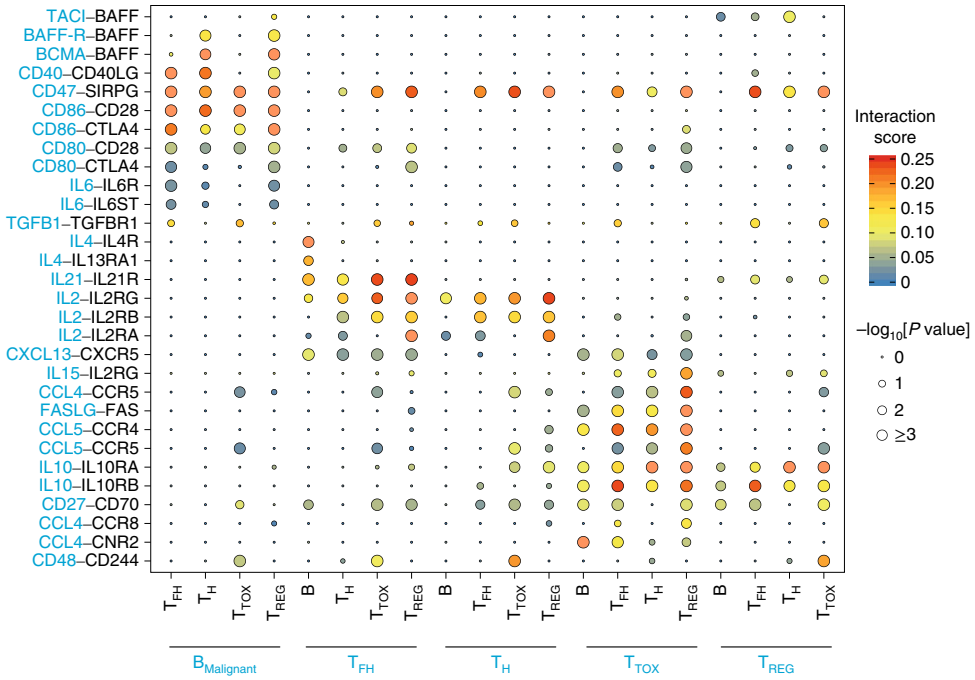

Fig. 4 | Cellular crosstalk in B-cell lymphomas in the lymph node microenvironment. Overview of the most significant ligand–receptor interactions across $n = 8$ biologically independent lymphoma samples. The DLBCL1 sample was not included due to the low number of T cells. The circle size indicates the negative $\log_{10}$ of the adjusted *P* values. The *P* values were determined using a permutation test (see the Methods section for details on how the *P* values were calculated). The interaction scores were calculated as the mean expression of molecule 1 (blue, *y* axis) in cell type A (blue, *x* axis) and the mean expression of molecule 2 (black, *y* axis) in cell type B (black, *x* axis). Protein names instead of gene names were used for TACI (*TNFRSF13B*), BAFF-R (*TNFRSF13C*), BCMA (*TNFRSF17*) and BAFF (*TNFSF13B*). The statistical source data are provided.

we also observed strong interaction scores for T_{FH} via IL21–IL21R with malignant B cells and via IL2–IL2R with other T-cell subsets. This analysis supports our classification of T_{FH} cells as one of the four main T-cell subsets in the lymph node microenvironment and reveals that each subset may provide a distinct panel of stimuli to interact with malignant B cells.

Dissecting transcriptional intratumour heterogeneity using multicolour flow cytometry. Our next aim was to investigate different layers of intratumour heterogeneity. Unsupervised clustering of the scRNA-seq profiles of malignant and non-malignant B cells revealed that all of the malignant samples were composed of at least two transcriptionally distinct malignant subpopulations (Extended Data Fig. 5 and Supplementary Data 1). We aimed to validate scRNA-based clusters at the cellular level to examine their biological and clinical relevance. We therefore selected three samples (FL4, tFL1 and DLBCL1) based on the availability of material for follow-up studies. We inferred differentially expressed surface markers from the scRNA profiles and first validated the distinction of scRNA-based clusters by flow cytometry. In a second step, we cultured lymph node-derived lymphocytes with 58 different drugs at five different concentrations (Supplementary Table 4) and stained them with specific antibody combinations to assess their drug-response profiles by flow cytometry. In a third step, we sorted the subpopulations and performed genome sequencing for each subpopulation (tFL1 and DLBCL1).

Verifying five transcriptionally distinct clusters in a FL sample. Based on its scRNA profile, FL4 was composed of five different B-cell clusters (C1–C5; Extended Data Fig. 6a). To validate all five clusters at the cellular level, we stained the differentially expressed surface markers CD44, CD24, CD22, CD27, and κ and λ light chains (encoded by *IGKC* and *IGLC2*, respectively; Extended Data Fig. 6b). Using the ratio of *IGKC* and *IGLC2* (see the Methods section for details), we found non-malignant B cells in C1, λ-restricted malignant B cells in C2 and malignant B cells with only marginal expression of *IGKC* and *IGLC2* in C3–C5 (Extended Data Fig. 6c). The pattern of light-chain expression could be perfectly comprehended using flow cytometry (Extended Data Fig. 6d), enabling us to differentiate C1 versus C2 versus C3, C4 and C5. Cluster C3 could then be recognized by a high expression of CD44 (Extended Data Fig. 6d,e). To further distinguish C4 and C5 among the $CD44^{Low}$ cells, we combined CD22, CD27 and CD24 and detected a subpopulation with $CD22^{High}$, $CD27^{High}$ and $CD24^{Low}$, which corresponded to the expression pattern of cluster C5 (Extended Data Fig. 6f). This approach allowed us to proof all five scRNA-based clusters by flow cytometry with comparable frequencies.

To assess the subpopulation-specific drug responses, we stained for κ and λ light chains and focused on the two major populations (C2, λ^+ and C3–C5, κ/λ^-). Although we did not observe differential responses for the majority of the targeted drugs, we found that only the κ/λ^- subpopulation was sensitive to chemotherapeutics (Extended Data Fig. 6g). This observation might explain why this patient achieved only a partial remission after chemotherapy treatment.

The indolent and aggressive components of transformed FLs exhibit a distinct transcriptional, genomic and drug-response profile. For the tFL1 sample, we detected three transcriptionally distinct clusters of B cells (Fig. 5a,b). Two clusters exclusively contained malignant B cells and one cluster contained non-malignant B cells. Based on their gene-expression profiles, we assessed the proliferative activity and observed that only one malignant cluster contained cells in the S phase (Extended Data Fig. 7a), without cells in the G_2 or M phases (Extended Data Fig. 7b). This suggests that this cluster represents a proliferating and thus aggressive component

of the transformed FL. The GSEA on the expression differences between the two malignant clusters revealed that gene-expression signatures associated with MYC, MTORC1 and the G_2M transition[47] were significantly enriched in the presumptively aggressive subpopulation (Extended Data Fig. 7c–e).

Among the genes that were differentially expressed, we found *FCGR2B* (Fig. 5a), which encodes the surface receptor CD32B, to be exclusively expressed in the presumptively indolent subpopulation (Extended Data Fig. 7f). Thus, we confirmed the existence of three B-cell populations by flow cytometry (Fig. 5c; see Supplementary Fig. 1a for the gating strategy). CD10 was strongly positive in both malignant B-cell populations ($CD32^{High}$ and $CD32^{Low}$) but not in non-malignant B cells.

As described earlier, we measured the ex vivo drug responses separately for each subpopulation (Fig. 5d,e) and observed diverse drug-response profiles. The BTK inhibitors—ibrutinib, acalabrutinib and tirabrutinib—and the immunomodulatory imide drugs—pomalidomide and lenalidomide—were exclusively active in the $CD32^{Low}$ subpopulation, whereas the histone deacetylase (HDAC) inhibitors—panobinostat, romidepsin and vorinostat—were more active in the $CD32^{High}$ subpopulation.

We sorted the three B-cell subpopulations based on CD32 and CD10 expression, and performed WES on each subpopulation as well as on whole-tumour and germline samples. The copy-number profiles of both malignant subpopulations were very different, including exclusive aberrations of chromosomes 3, 4, 6, 10, 12, 15, 18 and X (Extended Data Fig. 7g). Only the $CD32^{Low}$ subpopulation harboured a trisomy 12 (Fig. 5f), which was confirmed by scRNA-seq data (Fig. 5g). Trisomy 12 has been associated with a better response to B-cell receptor (BCR)-signalling inhibitors[48], which was consistent with our observation that this subpopulation was more responsive to these drugs (Fig. 5d,e). We also detected 157 somatic single-nucleotide variants (SNV) in exonic regions, of which 25 (15.9%) or 24 (15.2%) were exclusively detected in the $CD32^{High}$ and $CD32^{Low}$ subpopulations, respectively (Fig. 5h and Supplementary Table 5). However, the majority of somatic SNVs were equally represented in both subpopulations, indicating a phylogenetic relationship. We compared the allele count of all exonic SNVs between all three B-cell populations and did not detect somatic SNVs in healthy B cells (Fig. 5i,j), which provides support for the validity of our sorting approach.

Together, scRNA-seq allowed us to identify different subpopulations in the same lymph node that were genetically and functionally distinct in clinically relevant aspects.

A subpopulation-specific CNV of MYC drives a distinct gene-expression and drug-response program. The DLBCL1 sample was collected from a patient with a chemotherapy refractory disease during progression but before re-treatment. Using scRNA-seq, we identified two distinct clusters of malignant B cells, which exhibited a high number of differentially expressed genes associated with diverse cellular programs (Fig. 6a,b), such as BCR signalling (*PRKCB* and *NFKB1I*), cytokine signalling (*LGALS9* and *IFITM1*), MAPK signalling (*RGS13* and *FBLN5*) and antigen processing (*PTPN22*, *SELL* and *CD48*). Among the genes that were differentially expressed, we found *CD48* and *SELL* (Extended Data Fig. 8a,b), which encode for the surface markers CD48 and CD62L, respectively. Flow cytometry analysis of CD48 and CD62L staining validated the two distinct subpopulations ($CD48^{High}CD62L^{+}$ and $CD48^{Low}CD62L^{-}$) at the cellular level (Fig. 6c). We measured the ex vivo drug responses for each subpopulation again (Fig. 6d,e) and observed a strikingly different drug-response profile between the two subpopulations: BCR-signalling inhibitors (acalabrutinib, tirabrutinib, ibutinib, duvelisib, idelalisib and entospletinib) and cyclin-dependent-kinase inhibitors were exclusively effective in the $CD48^{Low}CD62L^{-}$ subpopulation, whereas bromodomain-and-extra-terminal-motif (BET) inhibitors (I-BET-762 and OTX015), nucleoside analogues (cytarabine, fludarabine and cladribine) and vincristine were exclusively efficacious in the $CD48^{High}CD62L^{+}$ subpopulation.

We sorted viable tumour cells based on the surface markers CD48 and CD62L (Supplementary Fig. 1b) and performed WGS on each subpopulation as well as on whole-tumour and germline samples. We detected a total of 240 non-synonymous SNVs located in exonic regions (Supplementary Table 6); however, only one (0.4%) and five (2.1%) SNVs were exclusively detected in the $CD48^{Low}CD62L^{-}$ and $CD48^{High}CD62L^{+}$ clusters, respectively (Fig. 6f). We further compared the copy-number-variation (CNV) profiles of the two subpopulations: the $CD48^{High}CD62L^{+}$ cluster carried an additional copy of *MYC* located on chromosome 8q24 (Fig. 6g), which was reflected by increased expression levels of *MYC* (Extended Data Fig. 8c). Chromosome 14q harboured two copy number gains and one loss in the $CD48^{High}CD62L^{+}$ cluster (Fig. 6g). Moreover, chromosome X exhibited a copy number gain of the p arm in the $CD48^{High}CD62L^{+}$ cluster and a copy number loss of the q arm in the $CD48^{Low}CD62L^{-}$ cluster (Fig. 6g).

Given that pathological activation of MYC renders cells sensitive to BET inhibitors[49,50], we performed intracellular flow cytometry-based staining of MYC at baseline and after an incubation of 24 h with and without the two BET inhibitors I-BET-762 or OTX015. We confirmed an increase in the levels of *MYC* expression of the $CD48^{High}CD62L^{+}$ subpopulation at baseline (Fig. 6h and Extended Data Fig. 8d) and, as expected, found that *MYC* was downregulated following incubation with I-BET-762 (Extended Data Fig. 8e) and OTX015 (Extended Data Fig. 8f) but not following incubation with the BTK inhibitor ibrutinib (Fig. 6h and Extended Data Fig. 8g).

Fig. 5 | In-depth analysis of the sample tFL1. a,**b**, Single-cell transcriptomes of B cells derived from the tFL sample only (492 cells) were subjected to SNN-based clustering. **a**, The heatmap illustrates the top-30 genes that were differentially expressed between all three identified clusters. The gene-expression values were scaled to the maximum of each row. **b**, Clusters were colour-coded and visualized in t-SNE projections of the scRNA expression profiles of B cells. **c**, Lymph node cells derived from tFL1 were stained for viability, CD19, CD32 and CD10, and analysed by flow cytometry. The gates highlight three $CD19^{+}$ populations corresponding to the subclusters in **b**. The percentage of cells comprising these clusters is shown. The experiment was repeated three times with similar results. **d**,**e**, Unsorted cells from the tFL1 sample were incubated for 48 h with 58 drugs, each at five different concentrations, and stained as described above. Viability was normalized to the dimethylsulfoxide (DMSO) control for each subpopulation separately. **d**, The mean difference of viabilities between the two malignant subpopulations are shown. White indicates an equal response, whereas purple or green indicates a superior viability of the $CD32^{High}$ or $CD32^{Low}$ subpopulations, respectively. **e**, Six representative subpopulation-specific drug responses are shown: panobinostat, vorinostat and romidepsin (HDAC inhibitors); acalabrutinib (BCR-signalling inhibitor); and lenalidomide and pomalidomide (immunomodulatory imide drugs). **f**, WES was performed on fluorescence-activated-cell-sorted $CD32^{High}$ and $CD32^{Low}$ subsets as well as the non-malignant $CD10^{-}$ B-cell subset. The line plot shows the estimation of the total copy number for chromosome 12 for all three sorted populations. **g**, Density curves of single-cell gene-expression values for all genes located on chromosome 12 for each subpopulation. **h**–**j**, The scatter plots from the WES show the allele frequency of the mutated allele for exonic SNVs in both malignant subpopulations (**h**), $CD32^{Low}$ versus healthy B cells (**i**) and $CD32^{High}$ versus healthy B cells (**j**). The shaded purple and green boxes highlight SNVs that are exclusive to one of the malignant B-cell subpopulations. The red dots mark immunoglobulin-associated mutations. The legend at the top of the figure applies to all panels. The statistical source data are provided.

In vivo re-treatment confirms ex vivo prediction of the subpopulation-specific drug response. To exemplify the translational relevance of the subpopulation-specific drug responses, we performed WES of DLBCL1 during the second relapse after re-treatment with high-dose cytarabine. Based on ex vivo drug perturbation we had predicted that the CD48^{High}CD62L^{+}, but not the CD48^{Low}CD62L^{-}, subpopulation would respond to cytarabine (Fig. 6d). We compared several synonymous SNVs exclusive to the CD48^{High}CD62L^{+} subpopulation before re-treatment and during the second relapse, and observed that the cytarabine-sensitive subpopulation was successfully eradicated (Fig. 6i). Due to the lack of sufficiently exclusive SNVs in the resistant subpopulation, we took advantage of the loss of heterozygosity (LOH) on chromosome Xq (Fig. 6g) to determine the aberrant fraction of cells harbouring a loss

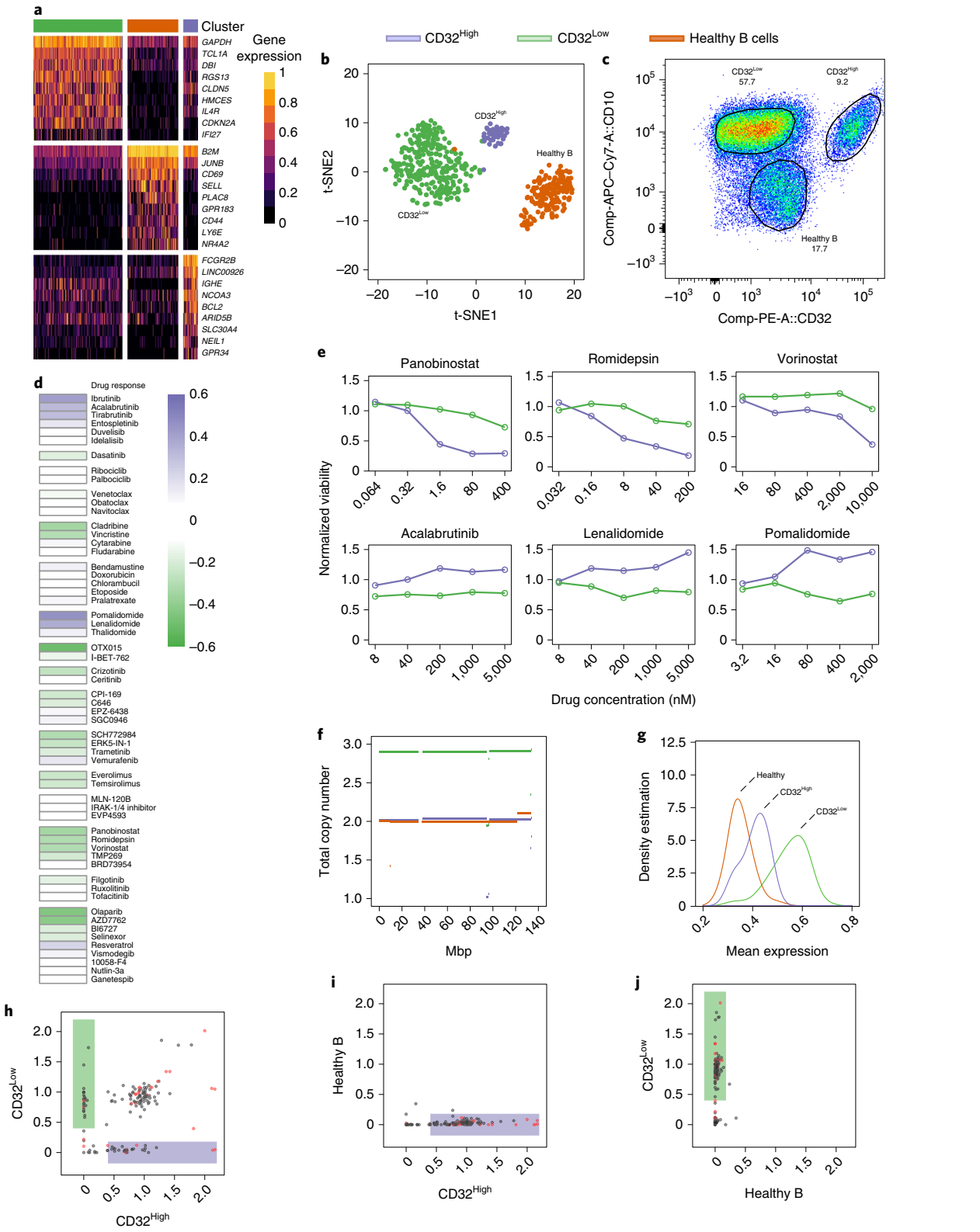

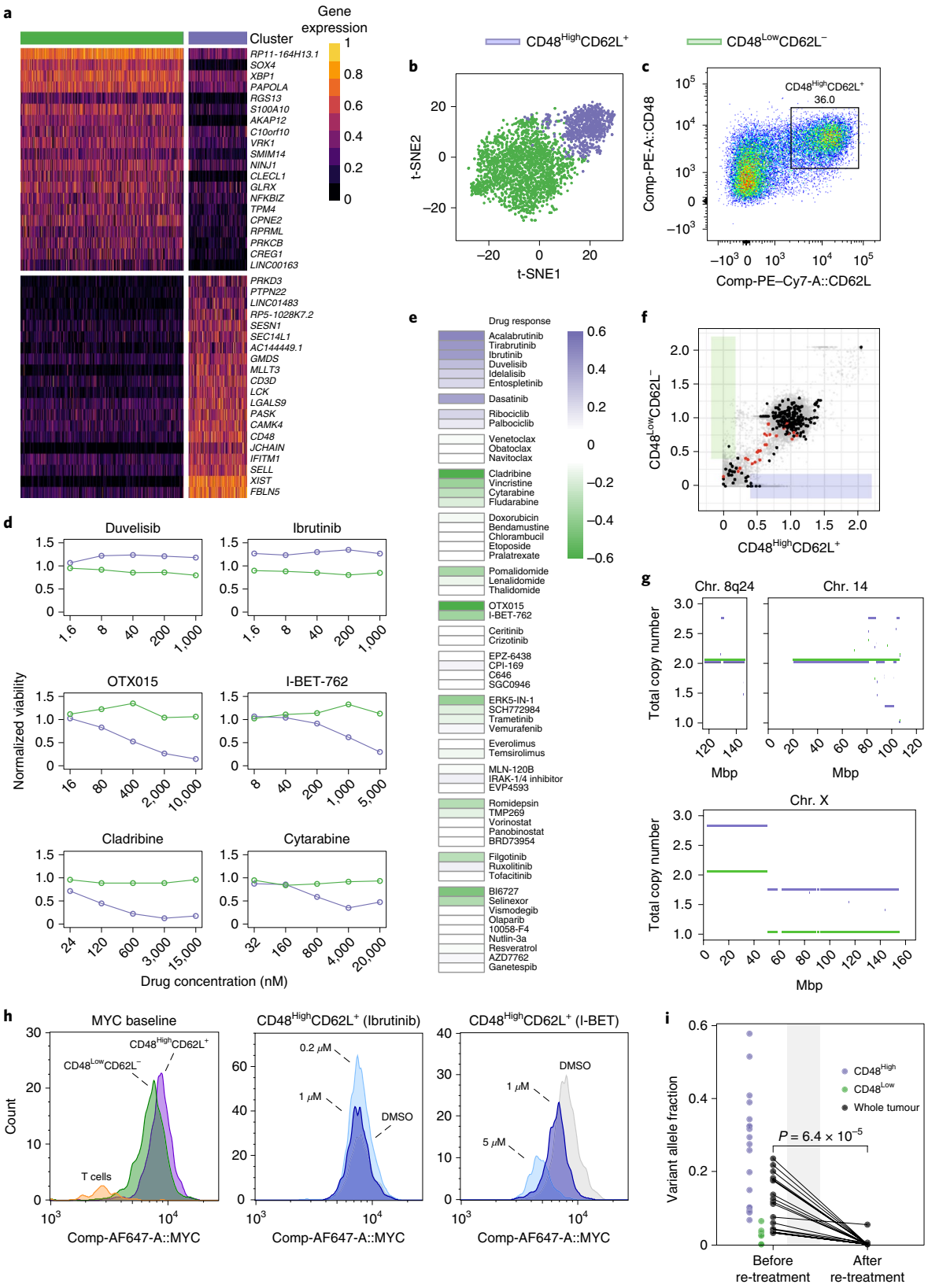

of Xq before and after re-treatment. We found that the fraction of chemotherapy-resistant cells, harbouring the loss of Xq, increased from 72 to 93% (see the Methods section for details).

In summary, we dissected the intratumour heterogeneity of the DLBCL1 sample at the transcriptional, genomic and drug-response levels. This example highlights the clinical relevance of tumour subpopulations and their specific drug-response profile for personalized cancer treatments.

Discussion

In this study we combined scRNA-seq and flow cytometry to investigate the intratumour heterogeneity of nodal B-NHLs at the

Fig. 6 | In-depth analysis of the sample DLBCL1. a,**b**, Single-cell transcriptomes of B cells derived from the DLBCL1 sample only (3,114 cells) were subjected to SNN-based clustering. **a**, Top-40 differentially expressed genes. The gene-expression values were scaled to the maximum of each row. **b**, Clusters were colour-coded and visualized in t-SNE projections of the scRNA expression profiles. **c**, DLBCL1-derived cells were stained for viability, CD19, CD48 and CD62L (SELL), and analysed by flow cytometry. The gating recapitulates the subpopulations identified in **a** and **b**. The experiment was repeated three times with similar results. **d**,**e**, DLBCL1-derived cells were incubated for 48 h with 58 drugs, each at five different concentrations, and stained as described in **c**. Viability was normalized to the DMSO controls for each subpopulation separately. **d**, Six representative subpopulation-specific responses are shown: I-BET-762 and OTX015 (BET inhibitors); ibrutinib and duvelisib (BCR-signalling inhibitors); and cytarabine and cladribine (chemotherapy). **e**, Mean difference of viabilities between the two subpopulations. White indicates an equal response, whereas purple and green indicate a superior viability of the $CD48^{High}CD62L^{+}$ and $CD48^{Low}CD62L^{-}$ subpopulations, respectively. **f**,**g**, WGS was performed on both sorted subpopulations. **f**, Allele frequencies of the mutated allele for non-synonymous exonic (black), immunoglobulin-associated exonic (red) and synonymous or intronic (grey) SNVs. The shaded purple and green boxes highlight SNVs exclusive to either of the subpopulations. **g**, Estimation of the total copy numbers for chromosome 8q24 (top left), 14 (top right) and X (bottom) for both clones. **h**, DLBCL1-derived cells were incubated with DMSO, I-BET-762 or ibrutinib. The cells were stained for viability, CD19, CD3, CD48, CD62L and MYC or the respective isotype control at baseline and after 24 h. The histograms show the fluorescence intensity of MYC at baseline and after 24 h, as indicated. **i**, Variant-allele frequencies of 21 independent SNVs in both subpopulations and whole-tumour samples before and after high-dose cytarabine treatment in vivo. The *P* value was calculated using a two-sided Wilcoxon test. The statistical source data are provided.

transcriptional, genetic and drug-response levels. Our analysis revealed the coexistence of up to four transcriptionally distinct subpopulations of malignant cells in individual B-NHL samples. This result recapitulates similar observations in FL[51], multiple myeloma[52] and other cancer entities[9,14,53]. We went further and established a straightforward strategy to prove the coexistence of up to four different tumour subpopulations at the cellular level. Moreover, we observed that tumour subpopulations in the same lymph node responded strikingly differently to targeted compounds and chemotherapeutics, which parallels observations in acute myeloid leukaemia with subclonal FLT3 mutations[54]. In addition, our approach could even predict the in vivo treatment sensitivity and resistance of tumour subpopulations in an example patient. Although we applied our approach to a limited number of malignant samples, it highlights the importance of identifying rational combinations of cancer drugs that effectively target all coexisting tumour subpopulations to avoid the outgrowth of resistant tumours.

Our approach enabled us to directly identify genetic factors that underlie the transcriptional and drug-response differences between subpopulations. This distinguishes our work from a previous study of FL, which compared allele frequencies of bulk WES with the size of the subpopulations identified by scRNA-seq[51]. The authors found a correlation between genomic alterations and subclonal fractions and concluded that somatic mutations are associated with transcriptional differences. While this study provided only indirect evidence, we physically sorted tumour subpopulations and performed DNA sequencing separately for transcriptionally distinct subpopulations. We observed two different scenarios regarding somatic mutations: in the DLBCL1 sample we identified almost no somatic SNVs to be exclusive for one or the other subpopulation, whereas in the tFL1 sample we found up to 15% exclusive somatic SNVs in each subpopulation. We further compared the CNV profiles of the same tumour subpopulations and found that all subpopulations harboured significantly different CNV profiles, suggesting that copy number alterations represent an important layer of genetic heterogeneity. Although our results support the general idea that genetic events drive subpopulation-specific differences such as drug response, they also highlight the difficulty to predict drug responses based only on genome sequencing in clinical practice.

Exploring the heterogeneity of the immune microenvironment in B-NHLs has the potential to better stratify patients for treatment with immunotherapies. Here we identified four major transcriptionally distinct T-cell subpopulations: T_{TOX}, T_{REG}, conventional T_H and T_{FH} cells. Although these subsets displayed limited transcriptional heterogeneity across donors and disease entities, their frequencies varied significantly, suggesting that B-NHLs shape their microenvironment by regulating the recruitment of different T-cell subsets. This observation might be of clinical relevance because B-NHLs with very few infiltrating T cells have been reported to respond less well to immunotherapies[55].

Despite the rather small number of patients with B-NHL that were analysed, our study is of high clinical relevance. We demonstrated that the prospective identification of pre-existing transcriptionally distinct malignant subpopulations might be of diagnostic value to detect difficult-to-treat tumour subpopulations. In addition, our research establishes scRNA-seq as a key technology for precise molecular profiling of relapsed and refractory nodal B-cell lymphomas and facilitates the design of molecularly informed diagnosis and treatment strategies.

Online content

Any methods, additional references, Nature Research reporting summaries, source data, extended data, supplementary information, acknowledgements, peer review information; details of author contributions and competing interests; and statements of data and code availability are available at https://doi.org/10.1038/s41556-020-0532-x.

Received: 2 July 2019; Accepted: 10 May 2020;
Published online: 15 June 2020

References

1. Burrell, R. A., McGranahan, N., Bartek, J. & Swanton, C. The causes and consequences of genetic heterogeneity in cancer evolution. *Nature* **501**, 338–345 (2013).
2. Chapuy, B. et al. Molecular subtypes of diffuse large B cell lymphoma are associated with distinct pathogenic mechanisms and outcomes. *Nat. Med.* **24**, 679–690 (2018).
3. Swanton, C. Intratumor heterogeneity: evolution through space and time. *Cancer Res.* **72**, 4875–4882 (2012).
4. McGranahan, N. & Swanton, C. Clonal heterogeneity and tumor evolution: past, present, and the future. *Cell* **168**, 613–628 (2017).
5. Kim, I. S. & Zhang, X. H. One microenvironment does not fit all: heterogeneity beyond cancer cells. *Cancer Metastasis Rev.* **35**, 601–629 (2016).
6. Fridman, W. H., Pages, F., Sautes-Fridman, C. & Galon, J. The immune contexture in human tumours: impact on clinical outcome. *Nat. Rev. Cancer* **12**, 298–306 (2012).
7. Navin, N. et al. Tumour evolution inferred by single-cell sequencing. *Nature* **472**, 90–94 (2011).
8. Wang, Y. & Navin, N. E. Advances and applications of single-cell sequencing technologies. *Mol. Cell* **58**, 598–609 (2015).
9. Tirosh, I. et al. Dissecting the multicellular ecosystem of metastatic melanoma by single-cell RNA-seq. *Science* **352**, 189–196 (2016).
10. Gao, R. et al. Nanogrid single-nucleus RNA sequencing reveals phenotypic diversity in breast cancer. *Nat. Commun.* **8**, 228 (2017).
11. Yuan, J. & Sims, P. A. An automated microwell platform for large-scale single cell RNA-seq. *Sci. Rep.* **6**, 33883 (2016).
12. Islam, S. et al. Quantitative single-cell RNA-seq with unique molecular identifiers. *Nat. Methods* **11**, 163–166 (2014).
13. Milpied, P. et al. Human germinal center transcriptional programs are de-synchronized in B cell lymphoma. *Nat. Immunol.* **19**, 1013–1024 (2018).

14. Patel, A. P. et al. Single-cell RNA-seq highlights intratumoral heterogeneity in primary glioblastoma. *Science* **344**, 1396–1401 (2014).
15. Ramskold, D. et al. Full-length mRNA-seq from single-cell levels of RNA and individual circulating tumor cells. *Nat. Biotechnol.* **30**, 777–782 (2012).
16. Powell, A. A. et al. Single cell profiling of circulating tumor cells: transcriptional heterogeneity and diversity from breast cancer cell lines. *PLoS ONE* **7**, e33788 (2012).
17. Kim, C. et al. Chemoresistance evolution in triple-negative breast cancer delineated by single-cell sequencing. *Cell* **173**, 879–893 (2018).
18. Teras L. R. et al. 2016 US lymphoid malignancy statistics by World Health Organization subtypes. *CA Cancer J. Clin.* **66**, 443–459 (2016).
19. Wagner-Johnston, N. D. et al. Outcomes of transformed follicular lymphoma in the modern era: a report from the National LymphoCare Study (NLCS). *Blood* **126**, 851–857 (2015).
20. Crump, M. et al. Outcomes in refractory diffuse large B-cell lymphoma: results from the international SCHOLAR-1 study. *Blood* **130**, 1800–1808 (2017).
21. Philip, T. et al. High-dose therapy and autologous bone marrow transplantation after failure of conventional chemotherapy in adults with intermediate-grade or high-grade non-Hodgkin's lymphoma. *N. Engl. J. Med.* **316**, 1493–1498 (1987).
22. Bartlett, N. L. et al. Single-agent ibrutinib in relapsed or refractory follicular lymphoma: a phase 2 consortium trial. *Blood* **131**, 182–190 (2018).
23. Winter A. M., et al. A multi-institutional outcomes analysis of patients with relapsed or refractory DLBCL treated with ibrutinib. *Blood* **130**, 1676–1679 (2017).
24. Horna, P., Olteanu, H., Kroft, S. H. & Harrington, A. M. Flow cytometric analysis of surface light chain expression patterns in B-cell lymphomas using monoclonal and polyclonal antibodies. *Am. J. Clin. Pathol.* **136**, 954–959 (2011).
25. Challa-Malladi, M. et al. Combined genetic inactivation of β2-Microglobulin and CD58 reveals frequent escape from immune recognition in diffuse large B cell lymphoma. *Cancer Cell* **20**, 728–740 (2011).
26. Schreiber, R. D., Old, L. J. & Smyth, M. J. Cancer immunoediting: integrating immunity's roles in cancer suppression and promotion. *Science* **331**, 1565–1570 (2011).
27. Xu-Monette, Z. Y., Zhou, J. & Young, K. H. PD-1 expression and clinical PD-1 blockade in B-cell lymphomas. *Blood* **131**, 68–83 (2018).
28. Sun, L. L. et al. Anti-CD20/CD3 T cell-dependent bispecific antibody for the treatment of B cell malignancies. *Sci. Transl. Med.* **7**, 287ra270 (2015).
29. Os, A. et al. Chronic lymphocytic leukemia cells are activated and proliferate in response to specific T helper cells. *Cell Rep.* **4**, 566–577 (2013).
30. Becht E. et al. Dimensionality reduction for visualizing single-cell data using UMAP. *Nat. Biotechnol.* **37**, 38–44 (2019).
31. Schaerli, P. et al. CXC chemokine receptor 5 expression defines follicular homing T cells with B cell helper function. *J. Exp. Med.* **192**, 1553–1562 (2000).
32. Breitfeld, D. et al. Follicular B helper T cells express CXC chemokine receptor 5, localize to B cell follicles, and support immunoglobulin production. *J. Exp. Med.* **192**, 1545–1552 (2000).
33. Dorfman, D. M. & Shahsafaei, A. CD200 (OX-2 membrane glycoprotein) is expressed by follicular T helper cells and in angioimmunoblastic T-cell lymphoma. *Am. J. Surg. Pathol.* **35**, 76–83 (2011).
34. Weber, J. P. et al. ICOS maintains the T follicular helper cell phenotype by down-regulating Kruppel-like factor 2. *J. Exp. Med.* **212**, 217–233 (2015).
35. Yang, Z. Z. et al. PD-1 expression defines two distinct T-cell sub-populations in follicular lymphoma that differentially impact patient survival. *Blood Cancer J.* **5**, e281 (2015).
36. Byford, E. T., Carr, M., Ladikou, E., Ahearne, M. J. & Wagner, S. D. Circulating Tfh1 (cTfh1) cell numbers and PD1 expression are elevated in low-grade B-cell non-Hodgkin's lymphoma and cTfh gene expression is perturbed in marginal zone lymphoma. *PLoS ONE* **13**, e0190468 (2018).
37. Yamazaki, T., Nagumo, H., Hayashi, T., Sugane, K. & Agematsu, K. CD72-mediated suppression of human naive B cell differentiation by down-regulating X-box binding protein 1. *Eur. J. Immunol.* **35**, 2325–2334 (2005).
38. Klein, U., Rajewsky, K. & Kuppers, R. Human immunoglobulin (Ig)M^+IgD^+ peripheral blood B cells expressing the CD27 cell surface antigen carry somatically mutated variable region genes: CD27 as a general marker for somatically mutated (memory) B cells. *J. Exp. Med.* **188**, 1679–1689 (1998).
39. Hans, C. P. et al. Confirmation of the molecular classification of diffuse large B-cell lymphoma by immunohistochemistry using a tissue microarray. *Blood* **103**, 275–282 (2004).
40. Vento-Tormo, R. et al. Single-cell reconstruction of the early maternal–fetal interface in humans. *Nature* **563**, 347–353 (2018).
41. Shirota, H. et al. IL4 from T follicular helper cells downregulates antitumor immunity. *Cancer Immunol. Res.* **5**, 61–71 (2017).
42. Aguilar-Hernandez, M. M. et al. IL-4 enhances expression and function of surface IgM in CLL cells. *Blood* **127**, 3015–3025 (2016).
43. Peter-Martin, B. et al. Systematic investigation of microenvironmental drug resistance mechanisms in chronic lymphocytic leukemia. *Blood* **134**, 3363 (2019).
44. Spolski, R. & Leonard, W. J. IL-21 and T follicular helper cells. *Int. Immunol.* **22**, 7–12 (2010).
45. Gu-Trantien C. et al. CXCL13-producing TFH cells link immune suppression and adaptive memory in human breast cancer. *JCI Insight* **2**, e91487 (2017).
46. DiToro D. et al. Differential IL-2 expression defines developmental fates of follicular versus nonfollicular helper T cells. *Science* **361**, eaao2933 (2018).
47. Liberzon, A. et al. The Molecular Signatures Database (MSigDB) hallmark gene set collection. *Cell Syst.* **1**, 417–425 (2015).
48. Dietrich, S. et al. Drug-perturbation-based stratification of blood cancer. *J. Clin. Invest.* **128**, 427–445 (2018).
49. Delmore, J. E. et al. BET bromodomain inhibition as a therapeutic strategy to target c-Myc. *Cell* **146**, 904–917 (2011).
50. Chapuy, B. et al. Discovery and characterization of super-enhancer-associated dependencies in diffuse large B cell lymphoma. *Cancer Cell* **24**, 777–790 (2013).
51. Andor, N. et al. Single-cell RNA-seq of follicular lymphoma reveals malignant B-cell types and coexpression of T-cell immune checkpoints. *Blood* **133**, 1119–1129 (2019).
52. Ledergor, G. et al. Single cell dissection of plasma cell heterogeneity in symptomatic and asymptomatic myeloma. *Nat. Med.* **24**, 1867–1876 (2018).
53. Puram, S. V. et al. Single-cell transcriptomic analysis of primary and metastatic tumor ecosystems in head and neck. *Cancer Cell* **171**, 1611–1624 (2017).
54. de Boer, B. et al. Prospective isolation and characterization of genetically and functionally distinct AML subclones. *Cancer Cell* **34**, 674–689 (2018).
55. Li, J. et al. Tumor cell-intrinsic factors underlie heterogeneity of immune cell infiltration and response to immunotherapy. *Immunity* **49**, 178–193 (2018).

Publisher's note Springer Nature remains neutral with regard to jurisdictional claims in published maps and institutional affiliations.

© The Author(s), under exclusive licence to Springer Nature Limited 2020

Methods

Patients samples and lymph-node processing. Our study was approved by the Ethics Committee of the University of Heidelberg. Informed consent was obtained in advance. The study is compliant with all of the relevant ethical regulations regarding research involving human participants. The lymph nodes were cut into small pieces immediately after excision and placed in RPMI medium (Gibco) supplemented with 10% fetal bovine serum (FBS; Gibco), penicillin and streptomycin (Gibco) at a final concentration of 100 U ml^{-1} and 100 µg ml^{-1}, respectively, and L-glutamine (Gibco) at a final concentration of 2 mM. After filtering with a 40-µm strainer, the cells were washed once with PBS (Gibco), put in RPMI medium (Gibco) supplemented with 20% FBS (Gibco) and 10% DMSO (Serva) and then cryopreserved in liquid nitrogen until further analysis.

Quantification of IHC staining. Formalin-fixed lymph node tissues were processed through the routine IHC pipeline of the hospital and thereby stained for CD3, PAX5 and Ki67 (all Ventana). After completion of the diagnostics, the corresponding slides were scanned for a subset of patients ($n=7$). To quantify the frequencies of B and T cells, the open source software QuPath (v0.1.2) was used for PAX5-, CD3- and Ki67-stained slides according to the recommended workflow[56]. Following detection of about 100,000 cells per slide, the measurements were exported and further analysed using R. We visualized the intracellular signal of diaminobenzidine staining of all detected events in a histogram. We observed two clear peaks in the PAX5 and CD3 staining of all samples and set a threshold between the two peaks. Cells with an intracellular CD3 or PAX5 signal greater than this threshold were regarded as T or B cells, respectively. The proportion of Ki67$^+$ cells was obtained from routine pathology reports.

Surface and intracellular staining by flow cytometry. As described earlier, lymph node-derived cells were thawed and stained for viability using a fixable viability dye e506 (Thermo Fisher Scientific) and for different surface markers depending on the experimental set-up. The following surface antibodies were used: anti-CD3–PerCP–Cy5.5, anti-CD3–APC, anti-CD19–BV421, anti-κ–PE, anti-κ–FITC, anti-λ–PE–Dazzle, anti-CD22–APC, anti-CD24–BV785, anti-CD27–PE–Cy7, anti-CD32–PE, anti-CD44–PE, anti-CD48–PE, anti-CD62L–PE–Cy7, anti-CD10–APC–Cy7, anti-CD4–AF700, anti-CD8–FITC, anti-PD1–BV421 and anti-ICOS–PE–Dazzle (all BioLegend). In the case of subsequent intracellular staining, the cells were fixed and permeabilized with the intracellular fixation/permeabilization buffer set (Thermo Fisher Scientific) and stained with anti-MYC–AF647 (Thermo Fisher Scientific), anti-FoxP3–AF647 (BD Biosciences) or the adequate isotype controls (Thermo Fisher Scientific, BD Biosciences). The cells were then analysed using an LSR Fortessa (BD Biosciences) and FACSDiva (BD Biosciences, version 8). The gating strategy for the T-cell subsets is illustrated in Supplementary Fig. 2.

Estimating the proportions of malignant and non-malignant B cells by flow cytometry. Staining for the expression of light chains (κ and λ) is a well-established tool for the identification of the accumulation of light chain-restricted malignant B cells[57]. Lymph node-derived cells were stained as described earlier. If a population was comprised of more than 80% κ$^+$ or λ$^+$ B cells, we regarded this population as light chain-restricted and therefore malignant. We further assumed that the ratio of κ$^+$ versus λ$^+$ B cells among the possible remaining non-malignant B cells would still be balanced. Therefore, there must be roughly the same proportion of non-malignant B cells among those carrying the restricted type of light chain. This results in the following formula to estimate the proportion of malignant cells:

$$\text{Proportion}_{\text{B cells malignant}} \approx \text{Proportion}_{\text{B cells restricted}} - \text{Proportion}_{\text{B cells not restricted}}$$

In addition, cells without detectable expression of κ or λ light chains at the protein level were regarded as malignant cells because a loss of light-chain expression has not been observed in non-malignant lymph nodes[58].

Single-cell sample preparation and scRNA-seq. After thawing, cells were washed to remove DMSO as quickly as possible. We used a Dead cell removal kit (Miltenyi Biotec) for all samples to achieve a viability of at least 90%. The preparation of the single-cell suspensions, synthesis of complementary DNA and single-cell libraries were performed using a Chromium single cell v2 3′ kit (10x Genomics) according to the manufacturer's instructions. Each was sequenced on a single NextSeq 550 lane (Illumina).

Subpopulation-specific drug screening. Five different concentrations of 58 different drugs (Supplementary Table 4) and a suitable number of DMSO controls were prepared in 384-well plates. A DMSO concentration of 0.2% was used throughout. Lymph node cells were thawed in a water bath at 37 °C and the DMSO-containing freezing medium was removed as quickly as possible to reduce the cytotoxic effects. The lymph node cells were then rolled for 3 h in RPMI medium supplemented with penicillin and streptomycin (Gibco) at a final concentration of 100 U ml^{-1} and 100 µg ml^{-1}, respectively, L-glutamine (Gibco) at a final concentration of 2 mM and 10% human AB male serum (Sigma). The cells were seeded at a cell count of 50,000 cells in 50 µl per well. After 48 h, the cells were washed once with staining buffer (PBS (Gibco) supplemented with 1% FBS and 0.5% EDTA (Sigma Aldrich)). The cells were subsequently stained with Fixable viability dye e506 (Thermo Fisher Scientific), anti-CD3–APC, anti-CD19–BV421, and anti-CD48–PE, anti-CD62L–PE–Cy7 or anti-κ–FITC, anti-λ–PE–Dazzle, anti-CD10–APC–Cy7, anti-CD27–PE–Cy7, anti-CD32–PE (all BioLegend). After staining, the microtiter plate was washed twice with staining buffer. Next, the cells were fixed using paraformaldehyde at a final concentration of 2% for 15 min at room temperature and washed with staining buffer. The fixed cells were analysed using an LSR II and FACSDiva (BD Biosciences, version 8) equipped with a high throughput sampler system (BD Biosciences). Approximately 5,000–10,000 events were recorded per well. The flow cytometry data were analysed using the FlowJo software (Tree Star). The gating strategies are illustrated in Supplementary Fig. 1. We ruled out that significant up- or downregulation of subpopulation-discriminating surface antigens confound subpopulation-specific drug-response assessment by evaluating the fluorescence intensity of the corresponding markers before and after drug treatment (Supplementary Fig. 3).

FACS of B-cell subpopulations. Lymph node cells were stained as described earlier. Sorting was performed using a FACS Aria Fusion (BD Biosciences). We sorted either for e506$^-$CD3$^-$CD19$^+$CD48$^-$CD62L$^-$ and e506$^-$CD3$^-$CD19$^+$CD48$^+$CD62L$^+$ cells (DLBCL1) or e506$^-$CD3$^-$CD19$^+$CD10$^-$, e506$^-$CD3$^-$CD19$^+$CD10$^+$κ$^+$CD32^{low} and e506$^-$CD3$^-$CD19$^+$CD10$^+$κ$^+$CD32^{high} cells (tFL). The gating strategies are illustrated in Supplementary Fig. 1. All of the relevant fractions were analysed post sorting to confirm a purity of at least 95%.

WGS and WES. DNA was extracted using a DNeasy mini kit (Qiagen) according to the manufacturer's protocol, followed by quality control using gel electrophoresis and a TapeStation 2200 system (Agilent). Samples were prepared either for WGS or WES, as previously described[59]. Exome capturing was performed using the SureSelect human all exon V5 in-solution capture reagents (Agilent). If the samples were destined for WES on an Illumina HiSeq 2500 instrument, 1.5 µg genomic DNA was fragmented to an insert size of 150–200 bp using a Covaris S2 device, and 250 ng of Illumina adaptor-containing libraries were hybridized with exome baits at 65 °C for 16 h. If the samples were destined for WES on an Illumina HiSeq 4000 instrument, 200 ng genomic DNA was fragmented to an insert size of 300 bp using a Covaris LE220 or E220 device, and 750 ng of adaptor-containing libraries were hybridized with exome baits at 65 °C for 16 h. If the samples were destined for WGS on an Illumina HiSeq X instrument, 100 ng genomic DNA was fragmented to an insert size of 450 bp using a Covaris LE220 or E220 device, and libraries were prepared using the TruSeq nano kit (Illumina). Paired-end sequencing was carried out according to the manufacturer's recommendations on all platforms, yielding read lengths of 101 bp (HiSeq 4000) or 151 bp (HiSeq X).

Processing of scRNA-seq data. The Cell Ranger analysis pipeline (v2.1, 10x Genomics) was used to demultiplex the raw base-call files and convert them into FASTQ files. The FASTQ files were aligned to the reference genome (hg38) and filtered. The final number of cell barcodes, unique molecular identifiers (UMI) per cell, median genes and sequencing saturation are summarized in Supplementary Table 7.

Filtering and normalization of scRNA-seq data. The R package Seurat[60] (v2.3.3) was used to perform quality control and normalization. The gene count per cell, UMI count per cell and percentage of mitochondrial and ribosomal transcripts were computed using the functions of the Seurat package. Genes that were expressed in three or fewer cells were excluded from the downstream analysis. Libraries with a percentage of mitochondrial transcripts greater than 5%, along with those with fewer than 200 genes were filtered out before further analysis. As aggressive lymphomas displayed higher gene and UMI counts, the upper limit was set with regard to each sample. After the removal of low-quality cells, we analysed the scRNA-seq profiles of 35,957 cells with an average sequencing depth of approximately 1,400 genes per cell. Counts were adjusted for cell-specific sampling ('normalized') using the LogNormalize function with the default scale factor of 10,000.

Assessing the cell-cycle state using scRNA-seq data. The cell-cycle state was assessed using the gene set and scoring system described by Tirosh and colleagues[9]. Briefly, the S and G_2M scores were calculated based on a list of 43 S phase-specific and 54 G_2 or M phase-specific genes. The calculation of the actual scores was performed using the CellCycleScoring function of the Seurat R package.

Analysis of ligand–receptor interactions in scRNA-seq data. We used the CellPhoneDB database[40] as the basis for potential cell–cell interactions but expanded the list to include important B- to T-cell interactions (Supplementary Table 8). To assess the significance of each interaction, we adapted a statistical framework recently described by Vento-Tormo and colleagues[40] to our purpose. Importantly, we considered only genes that were expressed in 5% of at least one cell type.

Briefly, we performed pairwise comparisons between the different T- and B-cell subtypes for each ligand–receptor pair and sample. For each combination of two different cell types and each ligand–receptor pair, we permuted the cluster labels of cells at least 1,000 times and determined the mean interaction score (mean

expression of ligand in cell type A times the mean expression of receptor in cell type B). A *P* value was determined by calculating the proportion of permuted interaction scores that were by hazard higher than the actual interaction score. All interactions were calculated sample-wise. To determine which interactions were most relevant across different samples, we calculated the mean interaction scores and combined the different *P* values using the Fisher's method. The *P* values were then corrected using the Benjamini–Hochberg method. The R code is available on our GitHub repository (see the Code availability section).

Combining data from different samples and batch correction. After the identification of the different cell types, the datasets were split into non-B cells or B cells using the SubsetData function. The respective subsets were then combined using the MergeSeurat function. Putative batch effects between two runs were corrected using the mutual-nearest-neighbours technique[61], which was implemented in the scran Bioconductor package (v1.10.2).

Clustering and dimensionality reduction techniques. SNN-based clustering, t-SNE and UMAP visualization were performed using the FindClusters, RunTSNE and RunUMAP functions within the Seurat package[60]. Each of these were performed on the basis of a principal component analysis, which was performed using the RunPCA function of the Seurat package. The same parameters were applied to all samples. Because it is significantly faster than t-SNE and better preserves aspects of global structure in larger datasets[30], UMAP was used instead of t-SNE for combined datasets. Genes that were differentially expressed between the clusters were identified using the FindMarkers or FindAllMarkers functions in the Seurat package[60]. Genes that were differentially expressed between malignant B-cell clusters can be browsed interactively using an html file (see Data availability).

GSEA. Gene set enrichment analysis was performed using the GSEA java desktop application[62,63] and the Molecular Signatures Database (MSigDB, v6.2) provided by the Broad Institute[62,64]. Genes that were differentially expressed between two groups were used to determine significantly enriched gene sets.

WES and WGS data processing. Alignment of sequencing read pairs and variant calling were performed as recently described[65]. Briefly, reads were mapped to the human reference genome (hg19) using bwa-mem (version 0.7.8, minimum base quality threshold set to zero (-T 0), remaining settings left to default)[66]. Subsequently, reads were coordinate-sorted using bamsort (compression option set to fast) and duplicate read pairs were marked using bammarkduplicates (compression option set to best; both part of biobambam package version 0.0.148).

The SNVs and indels in matched tumour normal pairs were identified using the internal DKFZ variant calling workflows based on samtools/bcftools 0.1.19 with additional custom filters (optimized for somatic variant calling by deactivating the pval-threshold in bcftools) and Platypus 0.8.1, respectively, as described previously[65]. Gene annotation of variants was done using Annovar[67]. The variants were annotated with dbSNP141, 1,000 Genomes (phase 1), Gencode mapability track, UCSC High Seq Depth track, UCSC Simple-Tandem repeats, UCSC Repeat-Masker, DUKE-Excluded, DAC-Blacklist and UCSC Selfchain. These annotation tracks were used to determine a confidence score for each variant by a heuristic punishment scheme and only high-confidence variants were kept for further analysis. In addition, variants with strong read biases according to the strand bias filter were removed.

Genomic structural rearrangements were identified using the SOPHIA algorithm (unpublished, source code available at https://bitbucket.org/utoprak/sophia/). Briefly, supplementary alignments produced by bwa-mem were used as indicators of potential underlying structural rearrangements. Candidates were filtered by comparing them to a background control set of sequencing data obtained using normal blood samples from a background population database of 3,261 patients from published The Cancer Genome Atlas and International Cancer Genome Consortium studies as well as both published and unpublished studies of the German Cancer Research Center (DKFZ).

Allele-specific CNVs were detected using ACEseq (allele-specific copy number estimation from WGS)[68] for the WGS data and CNVkit for the WES data[69]. ACEseq determines absolute allele-specific copy numbers as well as tumour ploidy and tumour-cell content based on coverage ratios of tumour and control as well as the B-allele frequency of heterozygous single-nucleotide polymorphisms (SNPs). Structural rearrangements called by SOPHIA were incorporated to improve genome segmentation.

Multi-tumour comparison. To compare multiple tumour samples from the same donor, every SNV position was determined using samtools mpileup 1.6 for each sample. The variant-allele fraction at each of these SNV positions was determined by calculating the ratio between the number of variant reads and the total coverage at that position. To correct the variant-allele fraction for actual tumour-cell content, a scaling factor comprising ploidy and total copy number (TCN) estimates obtained from ACEseq/CNVkit was incorporated. Specifically, the scaling factor was obtained as the ratio between the purity-corrected number of alleles in the tumour ($TCN_{tumour} \times purity_{tumour}$) and purity-corrected total number of alleles in the sample ($(TCN_{tumour} \times purity_{tumour}) + 2 \times (1 - purity_{tumour})$).

Aberrant-cell-fraction estimation from LOH. To determine the aberrant-cell fractions, the minor-allele frequency (MAF; the ratio between the number of reads of the minor allele and total coverage at a given position) of a SNP was estimated for selected regions harbouring an LOH or a copy-number-neutral LOH (CN-LOH) in the tumour sample. Information on SNP location was received from matched-control SNV calling. To select heterozygous SNPs, only SNPs with a MAF ≥ 0.3 in the control were retained. Subsequently, the MAF values of the selected SNP were calculated for the tumour samples. For exome samples, only SNPs within the targeted capture regions were kept. The mean of the respective tumour MAF values was calculated and the aberrant cell fraction (ACF) was estimated as follows:

$$ACF_{CN-LOH} = 1 - 2 \times \text{mean}(MAF); ACF_{LOH} = \frac{1-2 \times \text{mean}(MAF)}{1-\text{mean}(MAF)}$$

Statistics and reproducibility. Statistical analyses were performed using R. The source data underlying statistical tests are available in the source data files linked to the figures.

Reporting Summary. Further information on research design is available in the Nature Research Reporting Summary linked to this article.

Data availability

The WGS and WES data have been deposited at the European Genome-phenome Archive (EGA). The EGA study accession ID is EGAS00001004335. The scRNA-seq data that support the findings of this study have been deposited in heiDATA under accession code VRJUNV. The single-cell expression data of merged B- and T-cell UMAP plots (Fig. 2a,b and Fig. 3a,b) are available for easy-to-use interactive browsing at https://www.zmbh.uni-heidelberg.de/Anders/scLN-index.html. Genes that were differentially expressed between B-cell clusters can be browsed in an interactive html file (Supplementary Data 1). All other data supporting the findings of this study are available from the corresponding author on reasonable request.

Code availability

The R codes used for data analysis are available at our GitHub repository without further restriction (www.github.com/DietrichLab/scLymphomaExplorer).

References

56. Bankhead, P. et al. QuPath: open source software for digital pathology image analysis. *Sci. Rep.* **7**, 16878 (2017).
57. Ratech, H. & Litwin, S. Surface immunoglobulin light chain restriction in B-cell non-Hodgkin's malignant lymphomas. *Am. J. Clin. Pathol.* **91**, 583–586 (1989).
58. Kaleem, Z., Zehnbauer, B. A., White, G. & Zutter, M. M. Lack of expression of surface immunoglobulin light chains in B-cell non-Hodgkin lymphomas. *Am. J. Clin. Pathol.* **113**, 399–405 (2000).
59. Heining, C. et al. NRG1 fusions in KRAS wild-type pancreatic cancer. *Cancer Discov.* **8**, 1087–1095 (2018).
60. Butler, A., Hoffman, P., Smibert, P., Papalexi, E. & Satija, R. Integrating single-cell transcriptomic data across different conditions, technologies, and species. *Nat. Biotechnol.* **36**, 411–420 (2018).
61. Haghverdi, L., Lun, A. T. L., Morgan, M. D. & Marioni, J. C. Batch effects in single-cell RNA-sequencing data are corrected by matching mutual nearest neighbors. *Nat. Biotechnol.* **36**, 421–427 (2018).
62. Subramanian, A. et al. Gene set enrichment analysis: a knowledge-based approach for interpreting genome-wide expression profiles. *Proc. Natl Acad. Sci. USA* **102**, 15545–15550 (2005).
63. Mootha, V. K. et al. PGC-1α-responsive genes involved in oxidative phosphorylation are coordinately downregulated in human diabetes. *Nat. Genet.* **34**, 267–273 (2003).
64. Liberzon, A. et al. Molecular signatures database (MSigDB) 3.0. *Bioinformatics* **27**, 1739–1740 (2011).
65. López, C. et al. Genomic and transcriptomic changes complement each other in the pathogenesis of sporadic Burkitt lymphoma. *Nat. Commun.* **10**, 1459 (2019).
66. Li, H. et al. The sequence alignment/map format and SAMtools. *Bioinformatics* **25**, 2078–2079 (2009).
67. Wang, K., Li, M. & Hakonarson, H. ANNOVAR: functional annotation of genetic variants from high-throughput sequencing data. *Nucleic Acids Res.* **38**, e164 (2010).
68. Kleinheinz K. et al. ACEseq—allele specific copy number estimation from whole genome sequencing. Preprint at *bioRxiv* https://doi.org/10.1101/210807 (2017).
69. Talevich, E., Shain, A. H., Botton, T. & Bastian, B. C. CNVkit: genome-wide copy number detection and visualization from targeted DNA sequencing. *PLoS Comput. Biol.* **12**, e1004873 (2016).

Acknowledgements

T.R. was supported by a physician scientist fellowship from the Medical Faculty of University Heidelberg. M.Seiffert was supported by a grant from the Deutsche Forschungsgemeinschaft (DFG). S.D. was supported by a grant from the Hairy Cell Leukemia Foundation, Heidelberg Research Centre for Molecular Medicine (HRCMM) and an e:med BMBF junior group grant and DFG through the SFB873 (project B7). The Anders laboratory was supported by the DFG via Collaborative Research Centre (CRC) 1366 (project number 394046768). For the data management, we thank the Scientific Data Storage Heidelberg (SDS@hd), which is funded by the state of Baden-Württemberg and a DFG grant (grant no. INST 35/1314-1 FUGG). We thank C. Kolb (University Hospital Heidelberg), M. Knoll (University Hospital Heidelberg), A. Lenze (University Hospital Heidelberg), the EMBL flow core facility and the EMBL gene core facility for their excellent technical assistance. We also thank the DKFZ Single-Cell Open Lab (scOpenLab) for the experimental assistance and J. Apel (heiDATA, University of Heidelberg) for assistance with data management. This study was also supported by the Heidelberg Centre for Personalized Oncology (DKFZ-HIPO). We thank the DKFZ Omics IT and Data Management Core Facility (ODCF) and the DKFZ Genomics and Proteomics Core Facility (GPCF) for their technical support.

Author contributions

T.R., M.B., M. Stolarczyk, J.-P.M., SA.H. and P.-M.B. performed experiments. T.R., J.S., A.U., F.F., M.B., N.A., H.B.-W., M.P., M. Schlesner and S.A. analysed the data. T.R., M.H., K.R., B.G., M. Seiffert, B.B., G.M., C.M.-T., S.F., W.H., S.A. and S.D. interpreted the data. T.R., T.Z., S.F. and S.D. designed the study. T.R., J.S., K.R., B.C., M. Schlesner, W.H., S.A. and S.D. wrote the paper.

Competing interests

The authors declare no competing interests.

Additional information

Extended data is available for this paper at https://doi.org/10.1038/s41556-020-0532-x.

Supplementary information is available for this paper at https://doi.org/10.1038/s41556-020-0532-x.

Correspondence and requests for materials should be addressed to S.D.

Reprints and permissions information is available at www.nature.com/reprints.

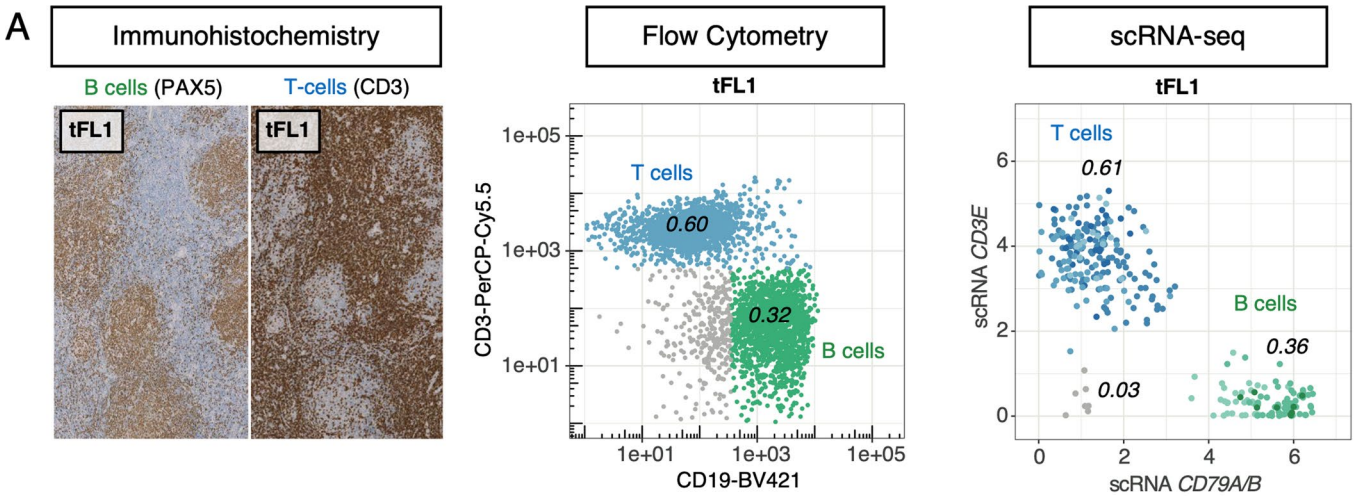

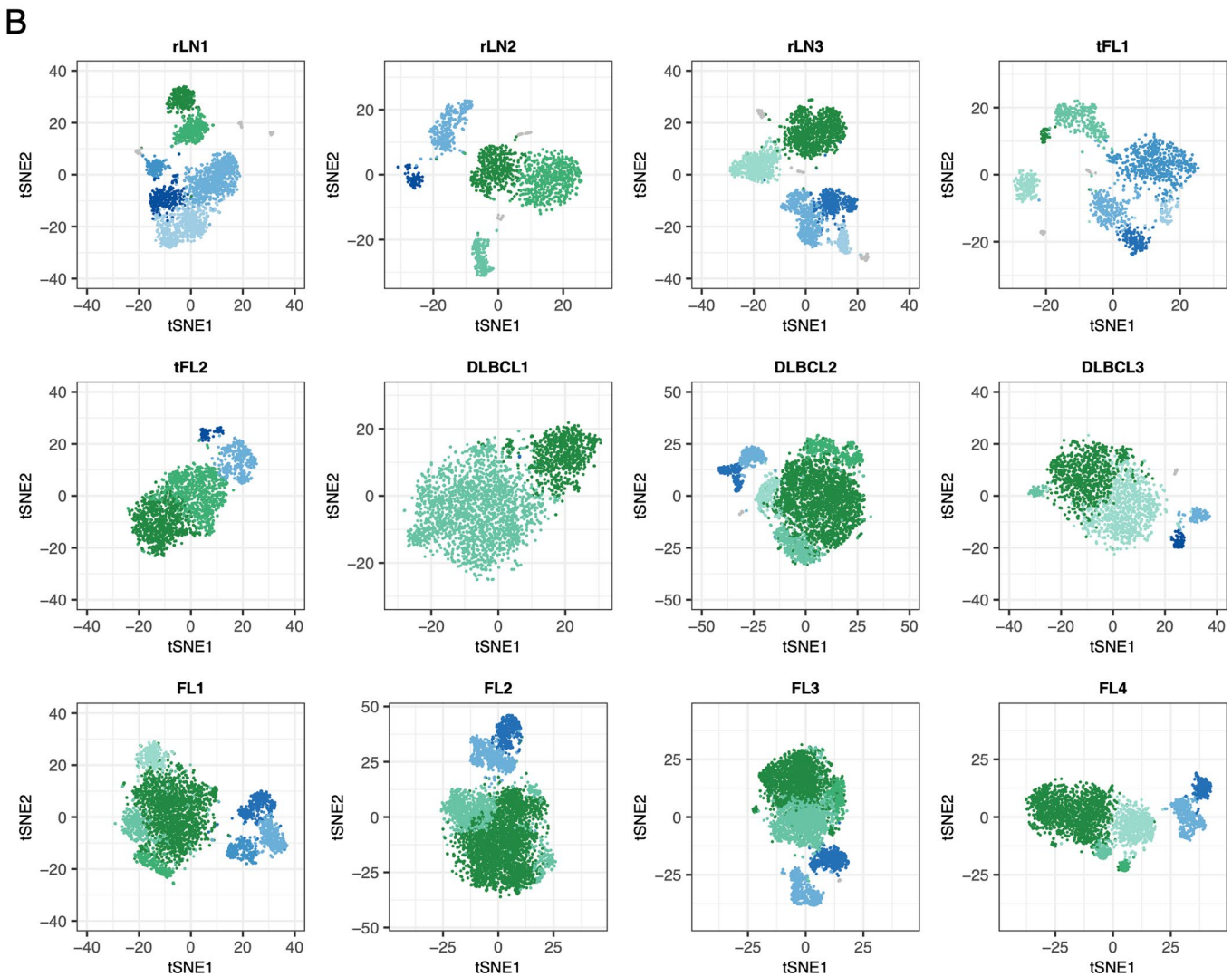

Extended Data Fig. 1 | Classification of B and T cells by scRNA-seq. a) Representative lymph node sample demonstrating how lymph node-derived B and T cells were classified by scRNA-seq (CD79B vs. CD3), flow cytometry (CD19 vs. CD3), or immunohistochemistry (PAX5 vs. CD3). Frequencies of B and T cells were determined for each approach in 12 (scRNA-seq, flow cytometry) or 7 (immunohistochemistry) biologically independent samples and correlated pairwise with each other (see main Fig. 1b and Fig. 1c). **b**) ScRNA-seq data of 12 biologically independent lymph node samples were subjected to SNN-based clustering and visualized by t-SNE. Each t-SNE represents one individual sample as indicated. Different B cell or T cell clusters are illustrated by different shades of green or blue, respectively. SNN: Shared-nearest-neighbour. See Source Data Extended Data Fig. 1.

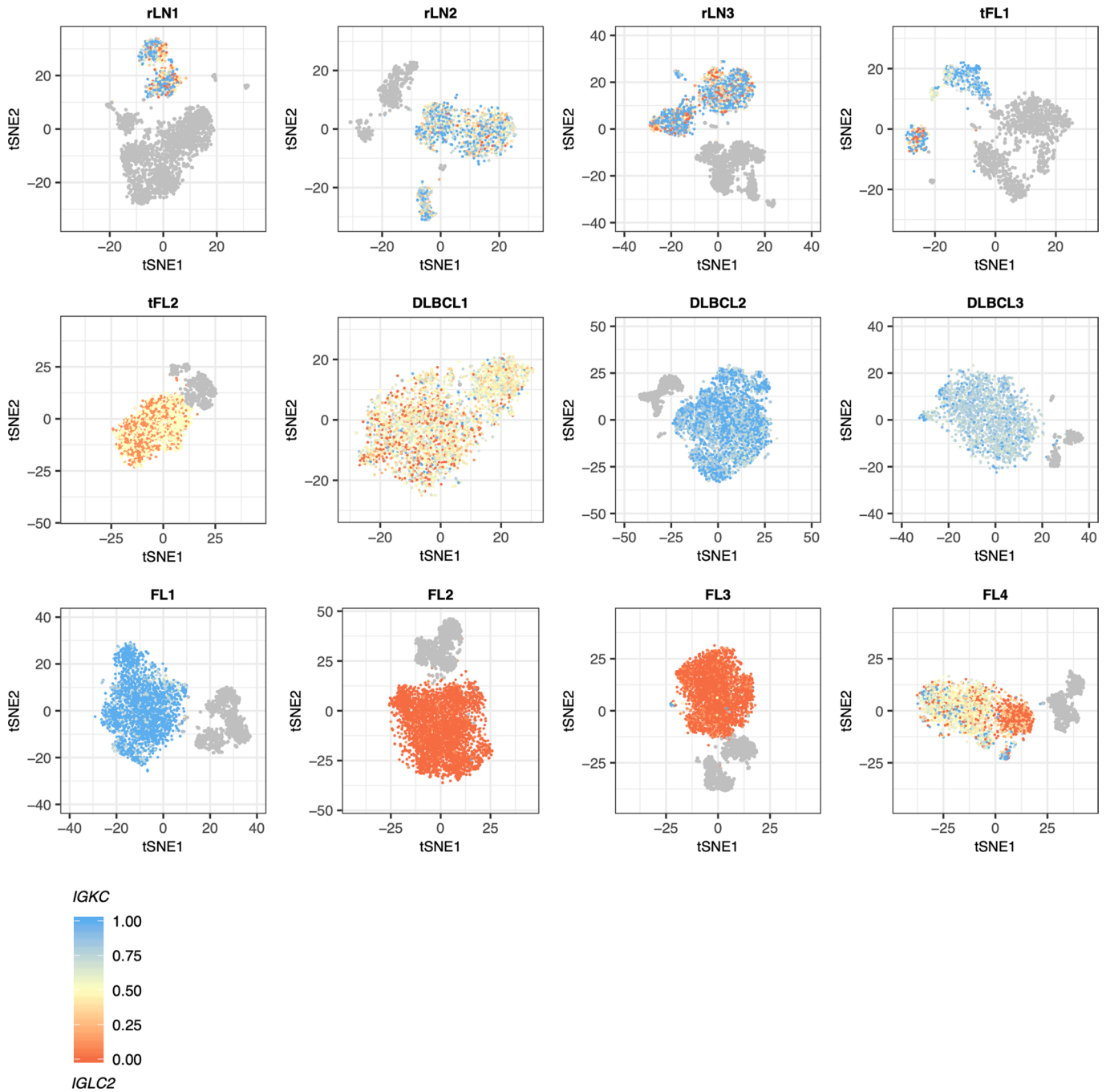

Extended Data Fig. 2 | Classification of malignant versus healthy B cells by means of kappa and lambda light chain expression at the scRNA level. scRNA-seq data of 12 independent lymph node samples were subjected to SNN-based clustering and visualized by t-SNE. Each t-SNE represents one individual sample as indicated. Cells are coloured by light chain kappa fraction *IGKC*/(*IGKC* + *IGLC2*) of each single cell to demonstrate light chain restriction of each cluster. Non-B cells are coloured in grey. The sample DLBCL1 showed only marginal light chain expression on single cell RNA level. Therefore, these cells were regarded as malignant cells (see Method section for details). The same is true for the larger cluster of sample FL4. SNN: Shared-nearest-neighbour. See Source Data Extended Data Fig. 2.

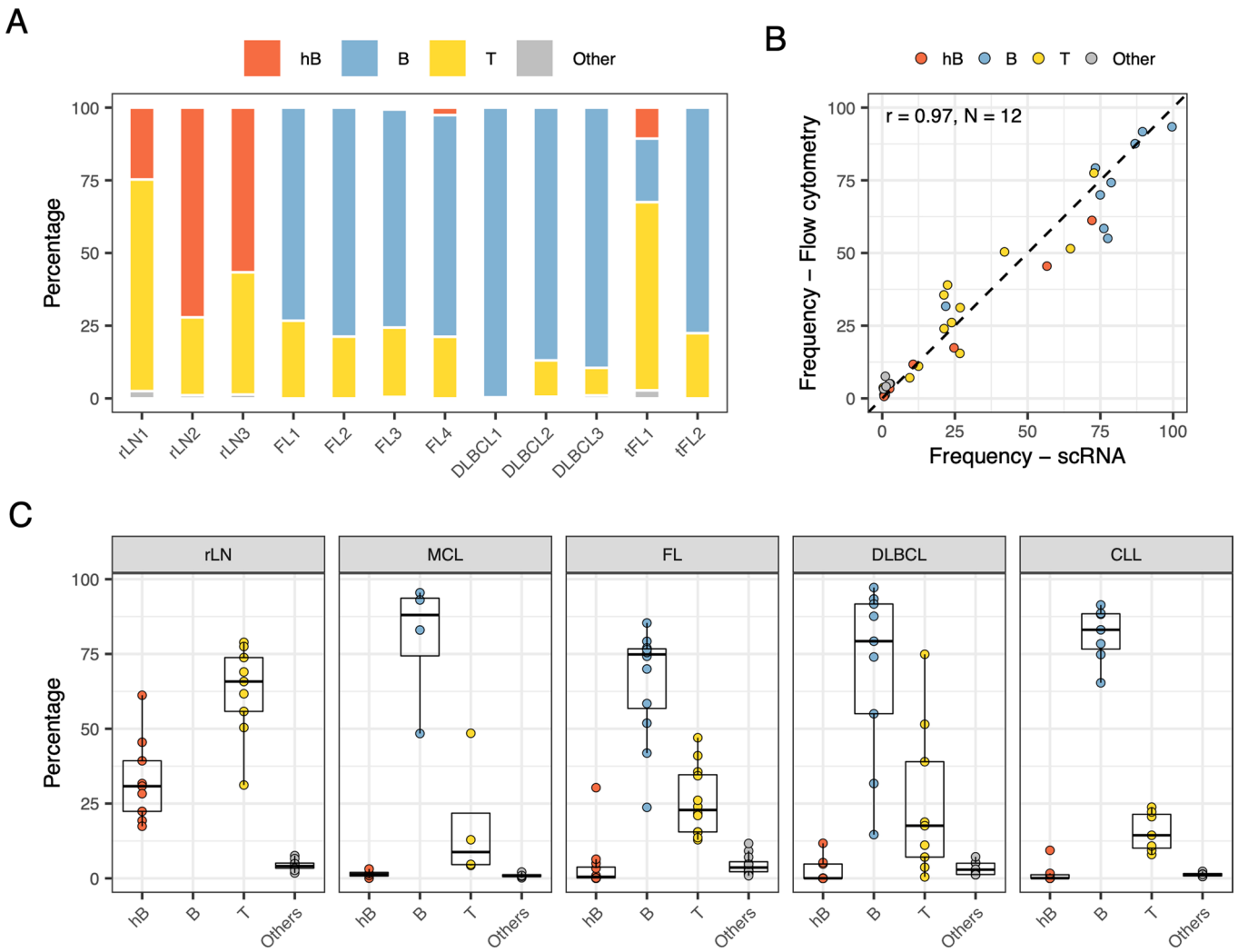

Extended Data Fig. 3 | Frequencies of T cells, healthy B cells and malignant B cells perfectly correlate between flow cytometry and scRNA-seq. **a**) Stacked bar graph of the relative frequencies of malignant B cells (B), T cells (T), healthy B cells (hB) and myeloid cells (Other) calculated on the basis of scRNA expression profiles. Shown are N = 12 biologically independent samples. **b**) Lymph node derived cells from those samples passed to scRNA-seq (A) were stained for viability, CD19, CD3, kappa light chain and lambda light chain. The proportion of healthy (hB) and malignant B cells (B) were estimated based on the ratio of light chain restricted $CD19^+$ tumour cells and $CD19^+$ non-tumour cells (malignant B cells = light chain restricted B cells – non-restricted B cells). T cells (T) refer to $CD3^+CD19^-$ cells, whereas Other refers to $CD19^-CD3^-$ cells. Pearson's correlation coefficients (r) are given. **c**) Lymph node derived cells were stained and analysed as described in B. Shown are the frequencies for each subpopulation for n = 9 (rLN), N = 4 (MCL), N = 11 (FL), N = 9 (DLBCL) and N = 7 (CLL) biologically independent samples. Box plots show the minimum, first quartile, median, second quartile and maximum. Outliers defined as values higher or lower than 1.5 interquartile ranges from median are shown as individual dots. rLN: Reactive lymph node. MCL: Mantle cell lymphoma. FL: Follicular lymphoma. DLBCL: Diffuse large B cell lymphoma, CLL: Chronic lymphocytic leukaemia. See Source Data Extended Data Fig. 3.

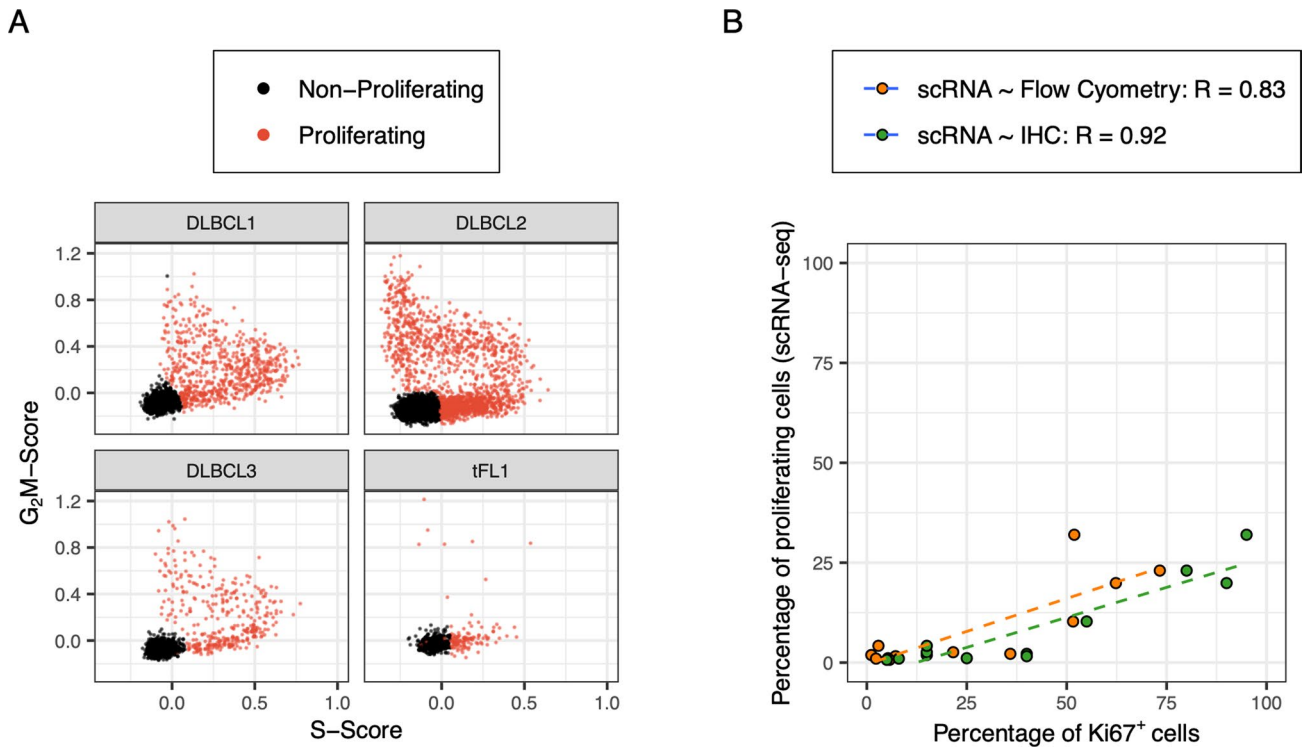

Extended Data Fig. 4 | Proliferative capacity is preserved at the scRNA level and correlates with immunohistochemical and flow cytometry-based staining of Ki67. a) Dot plots show G_2M and S score for the B cells of four representative samples. Cells with positive G_2M or S score were marked as proliferating (please see method section for details). **b**) The proportion of proliferating cells based on scRNA-seq (A) was correlated with the percentage of $Ki67^+$ cells determined either by flow cytometry (orange) or immunohistochemistry (green). R values represent Pearson correlation coefficients. N = 12 biologically independent samples are shown. See Source Data Extended Data Fig. 4.

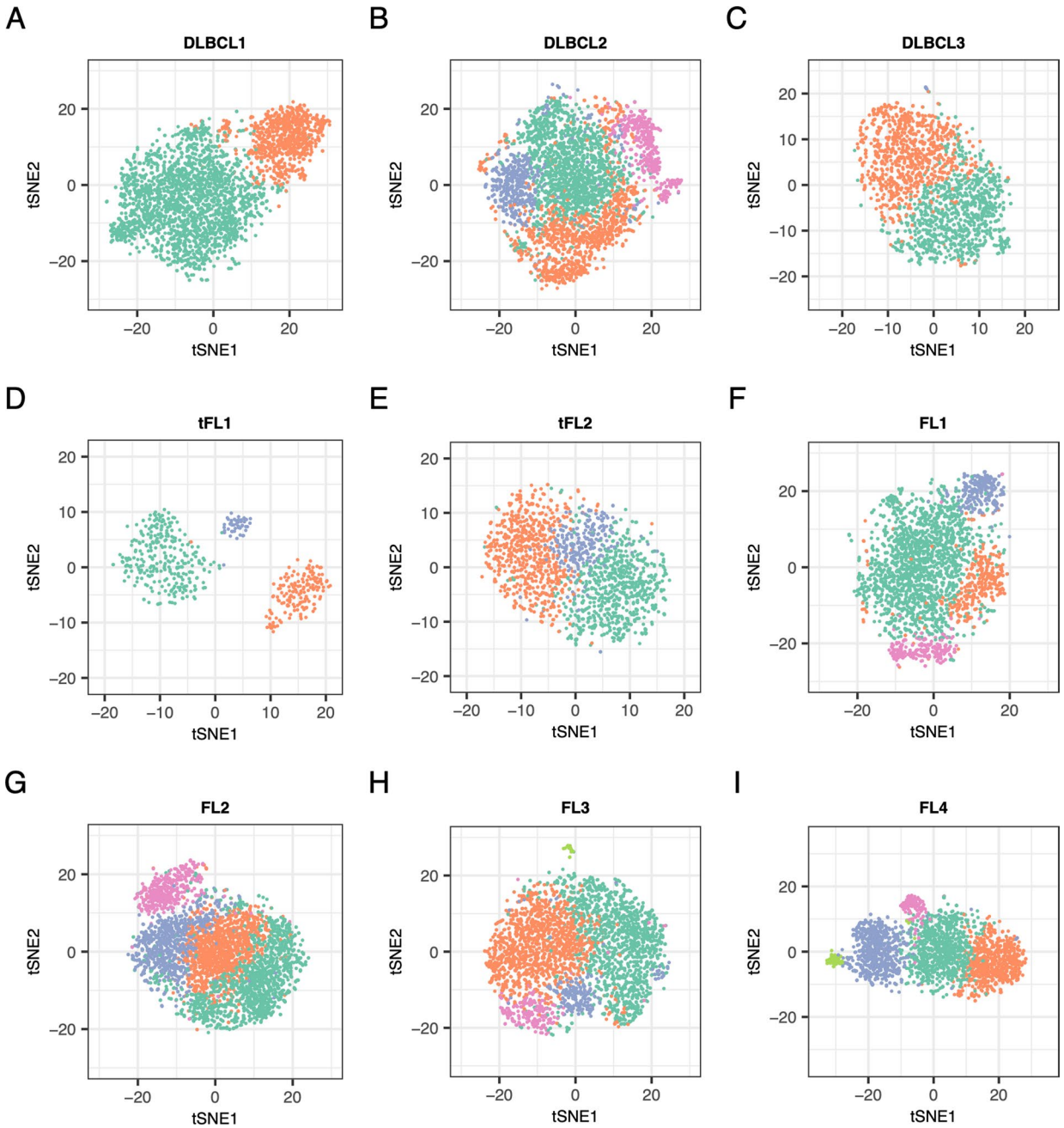

Extended Data Fig. 5 | intratumour heterogeneity of malignant B cells. a–i) ScRNA expression profiles of malignant and non-malignant B cells only were subjected to SNN-based clustering and visualized by t-SNE. Shown are 9 biologically independent samples, whereby each t-SNE represents one individual sample as indicated. Cells were coloured by cluster. SNN: Shared-nearest-neighbour. See Source Data Extended Data Fig. 5.

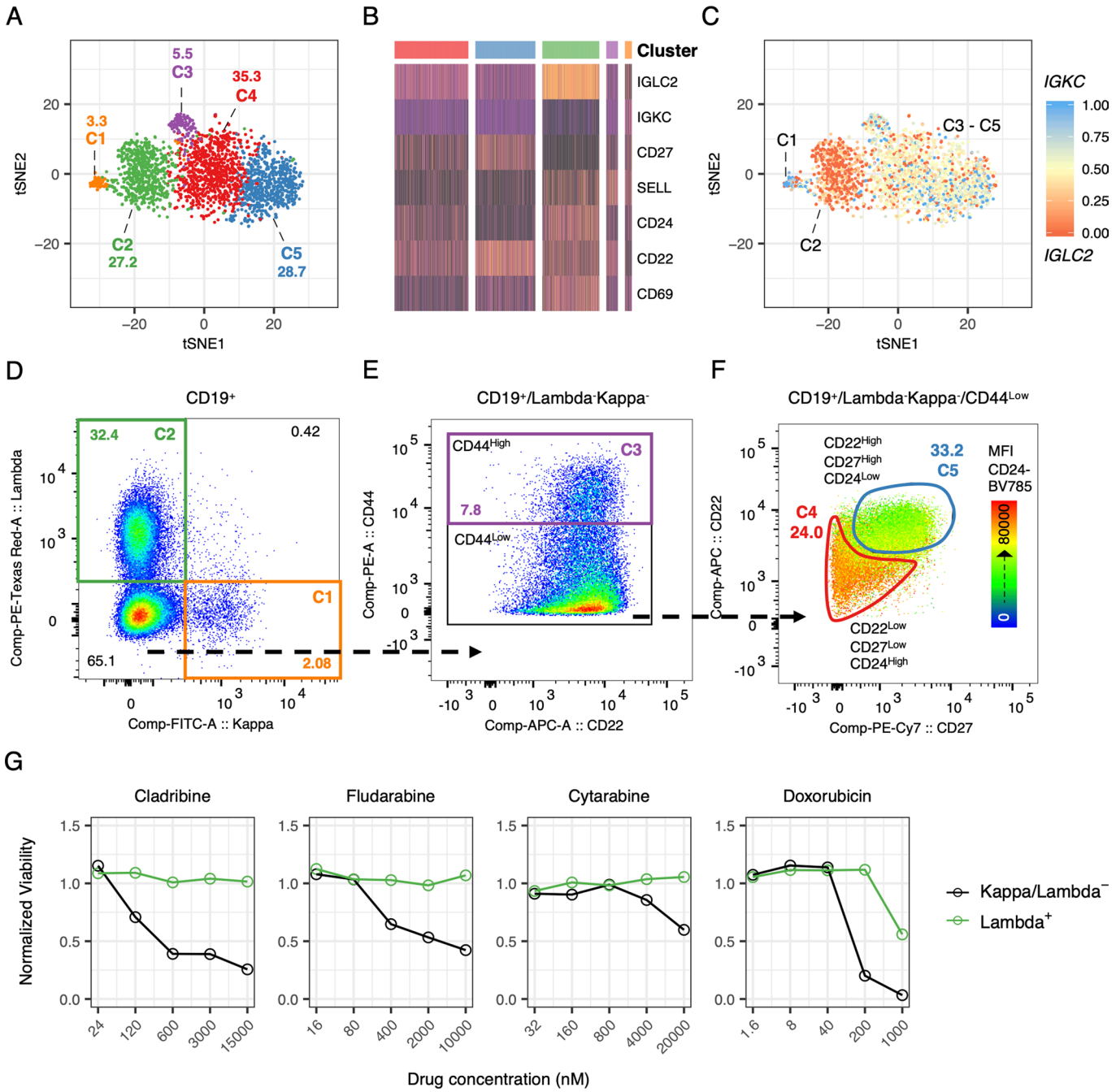

Extended Data Fig. 6 | Dissecting four distinct subpopulations of malignant B cells in FL4 sample by means of scRNA-seq-informed flow cytometry. **a**) ScRNA expression profiles of B cells from the FL4 sample only (2367 cells) were subjected to SNN-based clustering and visualized by t-SNE. **b**) Heatmap shows a selection of differentially expressed surface markers used for cluster differentiation. Gene expression values were scaled to the maximum of each row. **c**) T-SNE plot of panel A coloured by the light chain kappa fraction *IGKC*/(*IGKC* + *IGLC2*) of each single cell for FL4 sample only. C1 contains cells either expressing *IGKC* or *IGLC2* predominantly (benign B cells), C2 contains only cells expressing predominantly *IGLC2*, whereas C3 to C5 hardly express both *IGKC* and *IGLC2*. **d**–**f**) Cells derived from sample FL4 were stained for viability, CD3, CD19, kappa, lambda, CD44, CD24, CD22 and CD27. Shown is the stepwise gating strategy to comprehend the scRNA-seq-based clusters of panel A. **g**) Lymph node derived cells from the FL4 sample were incubated for 48 hours with 58 different drugs and 5 concentrations. Cells were stained for viability, CD3, CD19, kappa, lambda and CD27. Viability was normalized to DMSO controls for each subpopulation separately. Shows are only those drugs with significantly differential drug response between the two subpopulations. SNN: Shared-nearest-neighbour. DMSO: Dimethyl sulfoxide. See Source Data Extended Data Fig. 6.

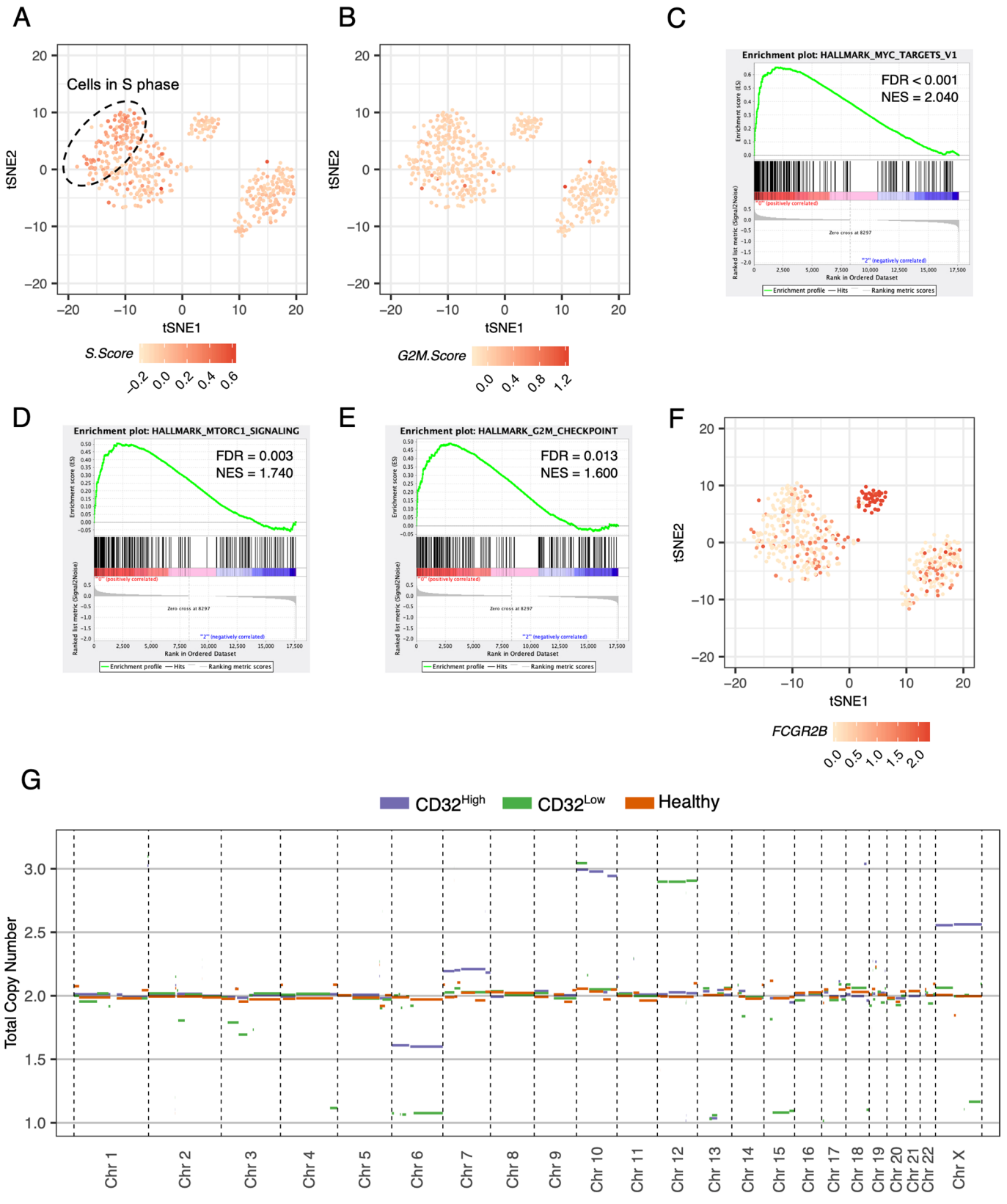

Extended Data Fig. 7 | Intratumour heterogeneity of tFL1 characterized by differential cell cycle states, gene expression signatures and copy number alterations. a, **b**) ScRNA expression profiles of B cells from the tFL1 sample only (492 cells) were subjected to t-SNE and coloured by S-Score (**a**) or G_2M-Score (**b**, see Methods section for details). **c**–**e**) Gene set enrichment analysis was performed between $CD32^{Low}$ and $CD32^{High}$ cluster. Shown are enrichment plots for hallmark MYC targets (**c**), MTORC1 signalling (**d**) and hallmark G_2M targets (**e**). Given are the false-positive detection rate (FDR) and the normalized enrichment score (NES). FDR and NES were calculated using GSEA desktop application (see Method section for details). **f**) T-SNE as shown in panel A/B was coloured by *FCGR2B* expression. **g**) Line plot shows cluster-specific total copy number estimation for all chromosomes inferred from whole exome sequencing. See Source Data Extended Data Fig. 7.

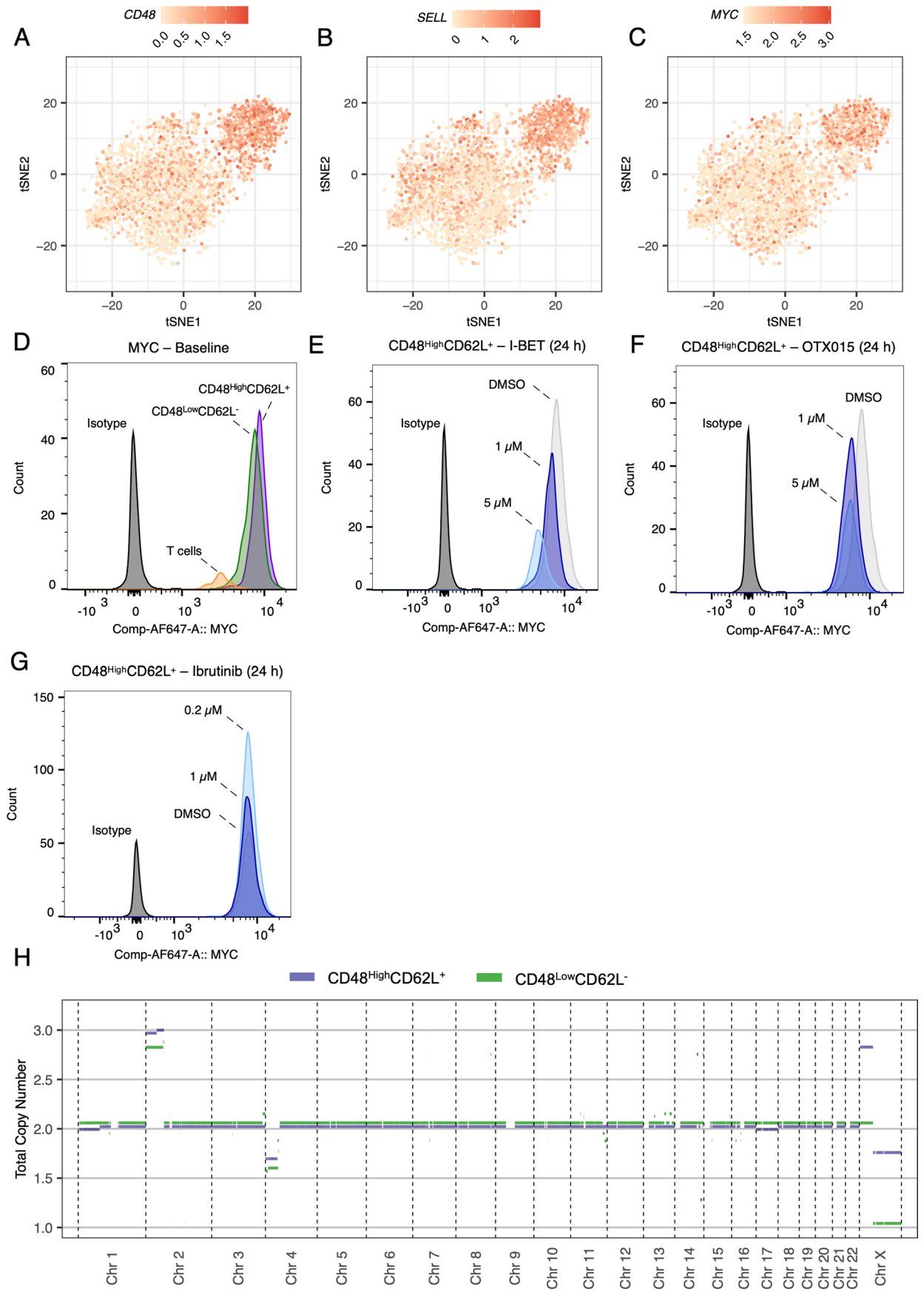

Extended Data Fig. 8 | See next page for caption.

Extended Data Fig. 8 | Intratumour heterogeneity of DLBCL1 sample. a–**c**) ScRNA profiles of malignant B cells from the DLBCL1 sample only (3114 cells) were subjected to t-SNE and coloured by CD48 (**a**), SELL (**b**) and MYC (**c**) expression. **d**) DLBCL1 derived lymph node cells were stained for viability, CD19, CD3, CD48, CD62L and MYC or respective isotype control. Histograms show fluorescence intensity of MYC for isotype control, T cells, $CD48^{High}CD62L^{+}$ and $CD48^{Low}CD62L^{-}$ subpopulations. Experiment was repeated three times with similar results. E-G) DLBCL1 derived lymph node cells were incubated with DMSO, I-BET-762 (**e**) at two concentrations (1 μM, 5 μM), OTX015 (**f**) at two concentrations (1 μM, 5 μM), or ibrutinib (**g**) at two concentrations (0.2 μM, 1 μM). After 24 hours, cells were harvested and stained as described in panel **d**. Histograms show fluorescence intensity for $CD48^{High}CD62L^{+}$ subclone. Experiment was repeated three times with similar results. H) Line plot shows total cluster-specific copy number estimation of DLBCL1 sample for all chromosomes as indicated using whole genome sequencing. DMSO: Dimethyl sulfoxide. See Source Data Extended Data Fig. 8.

nature research

Corresponding author(s): Sascha Dietrich

Last updated by author(s): Mar 27, 2020

Reporting Summary

Nature Research wishes to improve the reproducibility of the work that we publish. This form provides structure for consistency and transparency in reporting. For further information on Nature Research policies, see Authors & Referees and the Editorial Policy Checklist.

Statistics

For all statistical analyses, confirm that the following items are present in the figure legend, table legend, main text, or Methods section.

n/a	Confirmed
☐	☒ The exact sample size (*n*) for each experimental group/condition, given as a discrete number and unit of measurement
☐	☒ A statement on whether measurements were taken from distinct samples or whether the same sample was measured repeatedly
☐	☒ The statistical test(s) used AND whether they are one- or two-sided *Only common tests should be described solely by name; describe more complex techniques in the Methods section.*
☒	☐ A description of all covariates tested
☐	☒ A description of any assumptions or corrections, such as tests of normality and adjustment for multiple comparisons
☐	☒ A full description of the statistical parameters including central tendency (e.g. means) or other basic estimates (e.g. regression coefficient) AND variation (e.g. standard deviation) or associated estimates of uncertainty (e.g. confidence intervals)
☐	☒ For null hypothesis testing, the test statistic (e.g. *F*, *t*, *r*) with confidence intervals, effect sizes, degrees of freedom and *P* value noted *Give P values as exact values whenever suitable.*
☒	☐ For Bayesian analysis, information on the choice of priors and Markov chain Monte Carlo settings
☒	☐ For hierarchical and complex designs, identification of the appropriate level for tests and full reporting of outcomes
☐	☒ Estimates of effect sizes (e.g. Cohen's *d*, Pearson's *r*), indicating how they were calculated

Our web collection on statistics for biologists contains articles on many of the points above.

Software and code

Policy information about availability of computer code

Data collection	FACSDiva (BD Biosciences) Version 8 was used for acqusition of flow cytometry data.
Data analysis	Immunohistochemistry slides were analysed using the open source software QuPath (v0.1.2). Flow cytometry data were analysed using the commercial software FlowJo (Tree Star, v10). Single cell data were processed using the commercial software Cell Ranger (10x Genomics, v2.1). For data analysis and data visualization different R packages were used (open source): Seurat (v2.3.3, CRAN) and scran (1.12.1v, Bioconductor) for single cell data analysis. ggplot2 (v3.2.1, CRAN) and DT (v0.9) for data visualization. tidyr (v1.0.0, CRAN), dplyr (0.8.3.1v, CRAN), purrr (v0.3.3, CRAN) for data management. All R codes used for data analysis in the study are avaiable on our github repository and are accessible without restriction. For analysis of whole exome and whole genome sequencing data biobambam package (v0.0.148), samtools/bcftools (v0.1.19), Platypus (v0.8.1) and samtools mpileup (v1.6) was used (open source). Please find a detailed description in the method section. The software code is either already published (see references) or can be downloaded using the given bitbucket link. Gene set enrichment analysis (GSEA) was performed using the using the open source GSEA java desktop application and the Molecular Signatures Database (MSigDB, v6.2).

For manuscripts utilizing custom algorithms or software that are central to the research but not yet described in published literature, software must be made available to editors/reviewers. We strongly encourage code deposition in a community repository (e.g. GitHub). See the Nature Research guidelines for submitting code & software for further information.

Data

Policy information about availability of data

All manuscripts must include a data availability statement. This statement should provide the following information, where applicable:

- Accession codes, unique identifiers, or web links for publicly available datasets
- A list of figures that have associated raw data
- A description of any restrictions on data availability

The single cell count tables can be downloaded here https://doi.org/10.11588/data/VRJUNV. Data not included are available from the correesponding author upon reasonable request.

Field-specific reporting

Please select the one below that is the best fit for your research. If you are not sure, read the appropriate sections before making your selection.

☒ Life sciences ☐ Behavioural & social sciences ☐ Ecological, evolutionary & environmental sciences

For a reference copy of the document with all sections, see nature.com/documents/nr-reporting-summary-flat.pdf

Life sciences study design

All studies must disclose on these points even when the disclosure is negative.

Sample size	Sample sizes were not pre-determined; however, sample sizes were chosen based on other disease-related scRNA-seq studies referenced in the manuscript. We aimed to improve the understanding of intratumor heterogeneity in B cell lymphoma, and our data set is currently the largest invovling both aggressive and indolent B cell lymphoma, as well as non-malignant lymph nodes, particularly regarding the sparse avaiblability of viable lymph node samples. We investigated 13,259 malignant and 9,296 non-malignant. This number is sufficent to detect even rare cell types with a frequency below 1%.
Data exclusions	No data were excluded from the analysis.
Replication	All attempts of replication were successful.
Randomization	Not relevant - no treatment groups.
Blinding	Not relevant - no treatment groups.

Reporting for specific materials, systems and methods

We require information from authors about some types of materials, experimental systems and methods used in many studies. Here, indicate whether each material, system or method listed is relevant to your study. If you are not sure if a list item applies to your research, read the appropriate section before selecting a response.

Materials & experimental systems

n/a	Involved in the study
☐	☒ Antibodies
☒	☐ Eukaryotic cell lines
☒	☐ Palaeontology
☒	☐ Animals and other organisms
☐	☒ Human research participants
☒	☐ Clinical data

Methods

n/a	Involved in the study
☒	☐ ChIP-seq
☐	☒ Flow cytometry
☒	☐ MRI-based neuroimaging

Antibodies

Antibodies used	anti-CD3 rabbit monoclonal antibody (clone 2GV6, 0.04 µg per test, Ventana, 790-4341) anti-PAX5 rabbit monoclonal antibody (clone SP34, 0.04 µg per test, Ventana, 790, 4420) anti-Ki67 rabbit monoclonal antibody (clone 30-9, 0.04 µg per test, Ventana 790-4286) fixable viability dye e506 (Thermo Fisher Scientific, dilution 1:250, 65-0866-18) anti-CD3-PerCP/Cy5.5 (clone OKT3, dilution 1:50, Biolegend, 317336) anti-CD3-APC (clone HIT3a, dilution 1:50, Biolegend, 300312) anti-CD19-BV421 (clone HIB19, dilution 1:100, Biolegend, 302234) anti-kappa-PE (clone MHK-49, dilution 1:50, Biolegend, 316508) anti-kappa-FITC (clone MHK-49, dilution 1:50, Biolegend, 316506) anti-lambda-PE/Dazzle (clone MHL-38, dilution 1:50, Biolegend, 316621)

anti-CD32-PE (clone FUN-2, dilution 1:25, Biolegend, 303206)
anti-CD48-PE (clone BJ40, dilution 1:25, Biolegend, 336708)
anti-CD62L-PE/Cy7 (clone DREG-56, dilution 1:25, Biolegend, 304822)
anti-CD10-APC-Cy7 (clone HI10a, dilution 1:25, Biolegend, 312212)
anti-CD4-AF700 (clone RPA-T4, dilution 1:50, Biolegend, 300526)
anti-CD8-FITC (clone HIT8a, dilution 1:100, Biolegend, 300906)
anti-PD1-BV421 (clone EH12.2H7, dilution 1:25, Biolegend, 329919)
anti-ICOS-PE/Dazzle (clone C398.4A, dilution 1:50, Biolegend, 313532
anti-FoxP3-AF647 (clone 259D/C7, dilution 1:10, BD Biosciences, 560889)
anti-Ki67-BV786 (clone B56, dilution 1:50, BD Biosciences, 563756)
anti-CD22-APC (clone HIB22, dilution 1:25, Biolegend, 302510)
anti-CD24-BV785 (clone ML5, dilution 1:25, Biolegend, 311141)
anti-CD27-PE/Cy7 (clone O323, dilution 1:25, Biolegend, 302838)
anti-CD44-PE (clone BJ18, dilution 1:25, Biolegend, 338807)
anti-MYC-AF647 (clone 9E10, dilution 1:50 = 1 µg per test Thermo Fisher Scientific, MA1-980-A647)
mouse IgG1 isotype control AF647 (Thermo Fisher Scientific, 1 µg per test, MA5-18168)

Validation

Antibodies from Biolegend, BD Biosciences and Thermo Fisher Scientific are well-established standard monoclonal antibodies. Each antibody is quality control tested and validated by immunofluorescent staining with flow cytometric analysis as stated by the manufacturer. Additionally, we validated and titrated each of these antibodies by flow cytometric analysis using peripheral blood mononuclear cells from healthy donors.
Immunohistochemistry antibodies by Ventana are validated by immunofluorescent staining and analysis by Ventana.

Human research participants

Policy information about studies involving human research participants

Population characteristics	Supplementary Table 1 summarizes patient characteristics including diagnosis, diagnosis subtype, clinical situtation, age and gender. Samples used for scRNA-seq (n = 12) derive from patients with a median age of 62, were diagnosed as reactive lymphadenitis (3), follicular lymphoma (4) or diffuse large B cell lymphoma (5). 6 of them were male, 6 female. Among the patients with B cell lymphoma 3 were diagnosed initially, 6 had a relapse. Samples used for flow cytometry (n = 41) derive from patients with a median age of 64. Thery were diagnosed as reactive lymphadenitis (9), follicular lymphoma (12), mantle cell lymphoma (4), chronic lymphocytic leukaemia (7) or diffuse large B cell lymphoma (9). 29 of them were male, 12 female. Among the patients with B cell lymphoma 20 were diagnosed initially, 12 had a relapse.
Recruitment	Patient samples were selected based on the diagnosis (diffuse large B cell lymphoma, follicular lymphoma, mantle cell lymphoma, chonic lymphocytic leukemia, reactive/non-malignant lymph nodes) and the availability of viable lymph node-derived cells after processing the lymph node. It seems to be unlikely that this procedure introduces any selection bias as the cell yield is mainly influenced by the size of lymph node biopsy and this is determined by the surgical procedure.
Ethics oversight	Ethics Committee of the University of Heidelberg

Note that full information on the approval of the study protocol must also be provided in the manuscript.

Flow Cytometry

Plots

Confirm that:

☒ The axis labels state the marker and fluorochrome used (e.g. CD4-FITC).

☒ The axis scales are clearly visible. Include numbers along axes only for bottom left plot of group (a 'group' is an analysis of identical markers).

☒ All plots are contour plots with outliers or pseudocolor plots.

☒ A numerical value for number of cells or percentage (with statistics) is provided.

Methodology

Sample preparation	Human lymph node derived cells were thawed and subsequently stained for viability using a fixable viability dye e506 (Thermo Fisher Scientific) and for different surface markers depending on the experimental setup. In case of intracellular staining, cells were fixed using the intracellular fixation/permeabilization buffer set (Thermo Fisher Scientific).
Instrument	Immunophenotyping: LSR Fortessa (BD Biosciences) Flow cytometry-based drug screening: LSR II (BD Biosciences) Fluorescence-ativated cell sorting: FACSAria Fusion (BD Biosciences)
Software	Data collection: FACSDiva Version 8 (BD Biosciences) Data analysis: FlowJo (Tree Star)
Cell population abundance	All relevant post-sorting fractions were subsequently analyzed to confirm a purity of at least 95 %.

Gating strategy | For complete gating strategy of all relevant populations please see Extended Data Figure 6 and Supplementary Figure 1 and 2.

☒ Tick this box to confirm that a figure exemplifying the gating strategy is provided in the Supplementary Information.